学位論文（要約）

Interaction of Electromagnetic Waves with Electrons in Semiconductor Quantum Wells - Development of Ultra-Highly Sensitive THz Detectors

(半導体量子井戸構造中の電子と電磁波の相互作用の研究 - 超高感度テラヘルツ検出器の実現にむけて)

平成２６年１２月博士（理学）申請

東京大学大学院理学系研究科物理学専攻

二瓶　亮太

Abstract

In this thesis, we discuss level anti-crossing due to interaction between intersubband transition and LO phonons in the quantum-well structure. Spectral measurement by using charge sensitive infrared phototransistors (CSIP) has found evidence of strong resonant coupling of intersubband transition with LO phonons.

Our aim is to develop high sensitive CSIPs for astronomical applications in the wavelengths of 30 – 60 μm. Teraherz (THz) or Far-infrared (FIR) region ($\lambda \sim 30 - 300\ \mu$m) offers the opportunity to probe the characteristics of stars, planets, and galaxies. However, astronomical observations in 30 – 60 μm have been limited for the lack of sensitive detectors in this wavelength range.

CSIP is the promising detector with high sensitivity in the FIR region. This detector is a quantum-effect device implemented in a GaAs/AlGaAs double quantum-well (QW) structure. CSIP works as Field Effect Transistors (FET) consisting of both a photo-active part and read-out circuit. The floating gate is positively charged up by photo-excitation via intersubband transition. This mechanism gives extraordinary high photo-current responsivity ($> 10^5$ A/W). Adjusting the width of the QW can control the target wavelength (intersubband transition energy, ε_{12}).

Unfortunately, in GaAs there is the "Reststrahlen band" (33.8–36.8 μm at 4K). In the Reststrahlen band, the light is strongly reflected and absorbed due to strong coupling of photons with phonons. CSIP is, however, expected to exhibit finite response to the radiation in the Reststrahlen band since the photo-active region is well within the penetration depth (around a few microns) of radiation. Hence we designed and fabricated CSIPs for the target wavelength in the vicinity of the Reststrahlen band (32, 36 and 48 μm).

As a result, we observed photo-response in all the three devices. The spectral measurements revealed that the photo-response is located in two distinctly separated spectral region away from the target wavelength, one of which substantially overlaps with the Reststrahlen band.

In GaAs crystal, an electron in a QW repeats coherent process of virtual emission and absorption of LO phonons, leading to formation of a hybridized "polaron" state. The polaron states will give rise to level anti-crossing as the intersubband energy (ε_{12}) is close to the LO phonon energy (ε_{LO}). In order to quantitatively discuss the experimental results, we consider a theoretical model. The "dielectric continuum model" assumes a symmetric rectangular QW bounded by infinite barriers taking into account the interaction between electrons and LO phonons. The experimentally detected spectral energies were compared with the theoretical values with respect to dependence of the coupled-mode energies on the bare intersubband transition energy (ε_{12}) and on the two-dimensional electron density (N_{2DEG}) in the QW. The experimental values are substantially reproduced by the dielectric continuum model. This definitely indicates the validity of the interpretation described as formation of Polaron states.

This paper have reported detailed experimental evidence of the strong coupling between intersubband transition and LO phonons by using CSIPs. Thanks to high sensitivity and the unique structure of CSIP, we observed the both spectral branches due to anti-crossing in the QW structure for the first time. In order to develop CSIPs for the wavelengths of 30 – 60 μm, we have to pay careful attention to the strong coupling between intersubband transition and LO phonons.

This thesis is organized as follows: Chapter 1 describes that our interests in THz astronomy

and characteristics of CSIP. In Chapter 2, we indicate experimental methods and experimental results for spectral measurement at the wavelengths close to that of the Reststrahlen band. Chapter 3 discusses the cause of the spectral splitting with the comparison with theoretical models. Finally, conclusion is drawn in Chapter 4.

Contents

List of Tables

List of Figures

Chapter 1

Introduction

The progress of astronomy has been promoted by the development of detectors. It is also the case for the Terahertz (THz) astronomy. The Terahertz (THz) spectral region is a very important spectral domain in astronomy, since the domain is the repository of half the electromagnetic energy of galaxies. Development of sensitive THz detectors, however, is difficult because the frequencies are too high for heterodyne detectors and the photon energies are smaller than intrinsic band gap energies of semiconductors. Hence the same techniques established in the neighboring spectral bands cannot be applied to the THz detectors. As a result, the THz region remains as the final frontier in the wide frequency ranges from radio to γ-ray.

Recently, Komiyama et al. [1] introduced a new device called "Charge Sensitive Infrared Phototransistors" (CSIP), which is a promising candidate of sensitive THz detectors with performance needed in the future astronomical observations.

1.1 THz (Far-Infrared) Astronomy

In this thesis, we define THz range as that with the frequency range of 1-10 THz ($\lambda \sim 300$ – 30 μm), which is also called Far-infrared (FIR) region in astronomy. The THz or FIR region offers a unique opportunity to probe the process of star-, planet-, and galaxy-formation. Star-forming galaxies are heavily obscured by interstellar dust. Dust absorbs and re-radiates most of the energy originally released by young, hot stars, and the galaxies emit more than 90% of their total energy in the FIR [2] (Fig.1.1). Hence optical and near-infrared observations cannot reveal true nature of these galaxies due to heavy dust extinction. On the other hand, far-infrared observations can reveal the processes happening in these galaxies without much affected by dust extinction. One of the keys to reveal physical processes in these galaxies is FIR spectroscopy, offering rich lines which probe the characteristics of the interstellar medium in its ionized or neutral atomic and molecular phases. Measurements of these lines provide redshifts, gas masses, metal content, dust properties, and physical conditions from which luminosities, stellar populations, and star formation histories can be derived. notable examples of these lines are [SIII] 33μm, [SiII] 35μm, [NeIII] 36μm, [OI] 63μm, and [OIII] 52μm, 88μm [3].

Previous infrared space missions, e.g. Infrared Astronomical Satellite (IRAS) [4], Infrared Space Observatory (ISO) [5], Spitzer Space Telescope [6], AKARI [7], and Herschel Space Observatory [8], made significant contribution in the current astronomy by making the best use of the sensitive far-infrared observations in space. However, spectroscopic observations, especially in the wavelength range of 30 – 60 μm, have been very much limited due to the lack of sensitive detectors in this range. The wavelength range (30 – 60 μm) is especially important for the study protoplanetary disks, which are the key to understand the planetary-formation processes. A protoplanetary disk is a rotating circumstellar disk of dense gas surrounding a young newly formed

star. FIR spectrometry will allow us to reveal the physical and chemical evolution of the disc along the track of planetary formation. Figure1.2 shows a spectrum of the protoplanetary disk around young star HD142527 observed by the Infrared Space Observatory (ISO) [9]. The disk has emission features of H_2O water ice, which is expected to play essential roles both in energetics and in chemistry. Crystalline and amorphous water ices will show emission features at 44, 62 μm and at 46 μm, respectively [10] (Fig.1.3). FIR spectroscopy in this wavelength region can distinguish phase of H_2O water ices, leading us to prove the thermal history of the disk. Hence spectroscopic observations of protoplanetary disks at the wavelength range of 30 – 60 μm are expected to reveal physical and chemical evolution of protoplanetary disks related with planetary-formation processes.

Good spectroscopic observations require sensitive detectors. Hence, in this thesis, we focus on the highly sensitive detectors for the wavelength range of 30 – 60 μm, which has rich astronomical information yet unexplored.

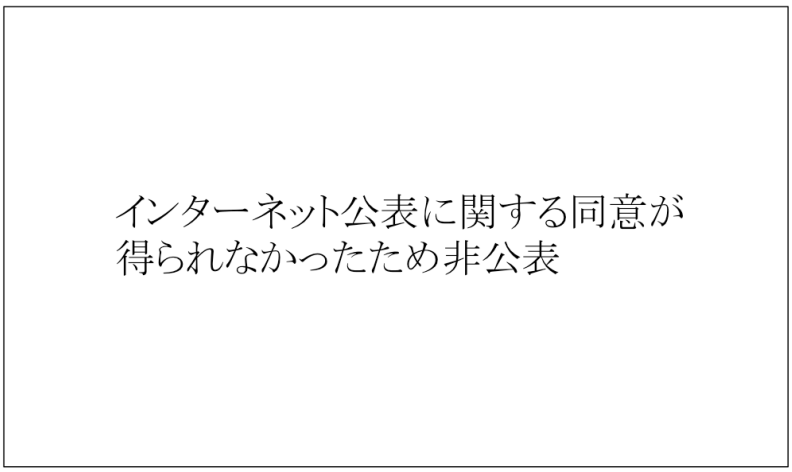

Figure 1.1: The spectral energy distribution of the galaxy M82 with two models (the solid and dashed curves) [11]. The vertical axis is the spectral flux density (Jansky, one Jansky corresponds to 10^{-26} W m^{-2} Hz^{-1}). M82 is the galaxy undergoing an exceptionally high rate of star formation (starburst galaxy), and is known as the closest starburst galaxy to our own Galaxy.

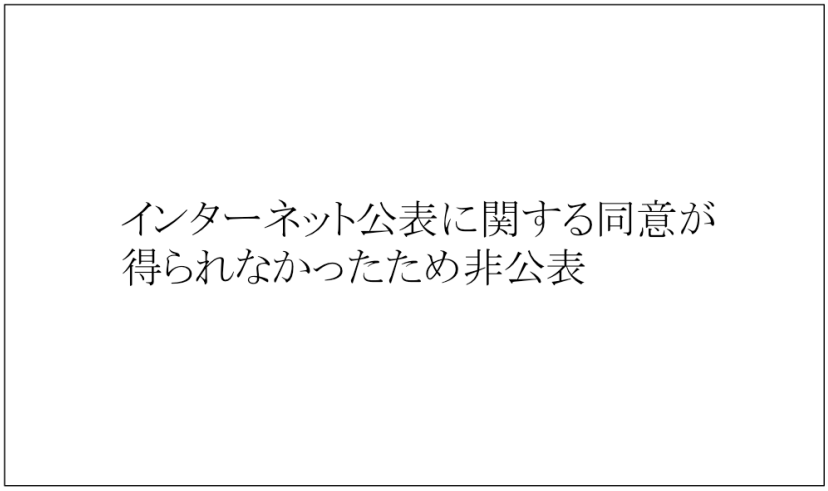

Figure 1.2: The spectrum of the young star HD 142527 observed by the Infrared Space Observatory (ISO) [9]. This spectrum shows the model components including the crystalline water ice features. The vertical axis is spectral flux density (Jansky).

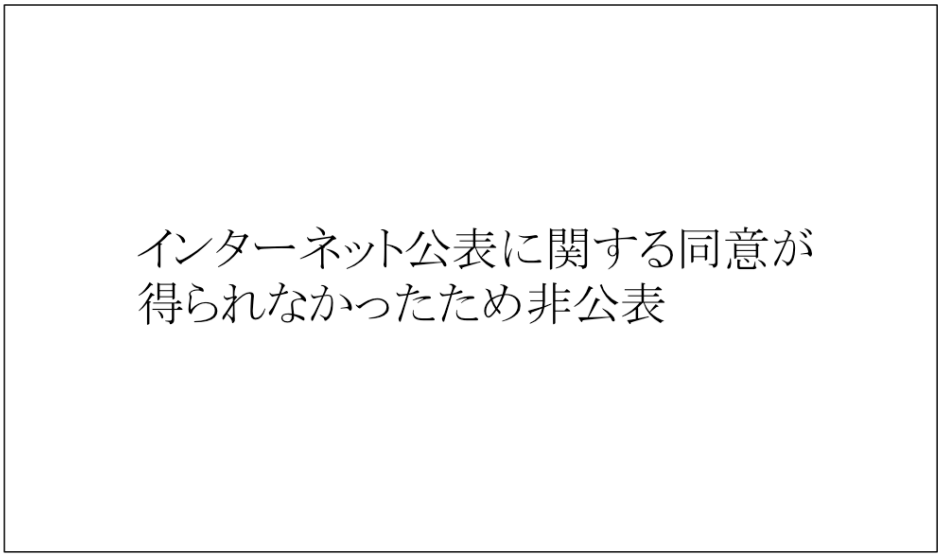

Figure 1.3: Imaginary part of the refractive index of crystalline H_2O ice (solid line) and amorphous H_2O ice (dashed line) between 2 – 100 μm [10]. This shows the positions of the major vibrational spectral features, i.e. the stretching, bending, librational (hindered rotation), and lattice (translational) features. Spectral features have significant differences between crystalline H_2O ice (44, 62 μm-band-peak) and amorphous (46 μm-band-peak) H_2O ice.

1.2 Charge Sensitive Infrared Phototransistor (CSIP)

Being situated between infrared light and microwave radiation, THz (or FIR) radiation is resistant to the commonly employed techniques in the well established neighboring radio and near- or middle-infrared (IR) regions. Therefore, THz range of electromagnetic spectrum still presents a challenge for both electronic and photonic technologies. The future THz spectroscopy, however, requires high sensitivity, in terms of noise equivalent power (NEP), $\sim 10^{-20}$ W/$\sqrt{\text{Hz}}$ to achieve the astrophysical photon noise limited performance. Recently, a few new devices approaching this requirement have been demonstrated. In the hopeful THz detectors, we focus our attention on the novel detector called "Charge Sensitive Infrared Phototransistors (CSIP)". CSIPs for the mid-infrared region ($\lambda = 15\ \mu$m) have reached NEP $\simeq 7 \times 10^{-20}$ W/$\sqrt{\text{Hz}}$ [1]. The characteristics of this detector are as follows:

- CSIP has GaAs/AlGaAs double quantum-well (QW) structures.
- CSIP is working as a phototransistor, that is, consisting of both a photo-active part and a read-out circuit.
- CSIP has amplification mechanism enough to detect a single photon.
- CSIP has spectral response at the mid-infrared region ($\lambda = 12 - 19\mu$m).
- CSIP works at cryogenic temperature of 4.2 K, demonstrated up to 23 K for the mid-infrared [12].

Moreover, easy-to-use due to large current responsivity along with remarkable sensitivity make CSIP a extremely promising detector for versatile applications. By tuning the design parameters of the wafer structure we can expand the target wavelength to longer region in principle. Thanks to the simple device structure, CSIP has promising potential to build large format arrays [13]. In the following subsections, details of CSIP are presented.

1.2.1 Intersubband transition within a quantum-well

In semiconductor materials, the radiation is usually absorbed via excitation of an electron from the valence band to the conduction band for visible or near infrared photon detectors. For far-infrared photons, smaller energy gaps are formed artificially, for example, by doping the impurity atoms into the pure semiconductor crystal like extrinsic photoconductors. For CSIP, forming nano-scale structures with compound semiconductors such as GaAs, energy levels of electron in a conduction band are quantized according to the structure parameters.

CSIP consists of GaAs and AlGaAs semiconductors. The difference of band gaps between GaAs (1.4 eV) and $Al_xGa_{1-x}As$ (1.6 – 1.8 eV, for x = 0.15 – 0.30), makes a quantum-well (QW) with subband levels in a conduction band. Subband energies in the QW is simply estimated assuming infinite potential well quantized in a one direction (z-direction). We thus have

$$\varepsilon_j = \left(\frac{\hbar^2 \pi^2}{2m^* L_{QW}^2} \right) j^2, \tag{1.1}$$

where m^* is a effective electron mass, L_{QW} is a width of the QW, and j is subband index. Given a intersubband transition from the ground state to the first excited state, by substituting $j = 1, 2$ into Eq. (1.1), the energy gap $\hbar\omega_{12}$ is

$$\hbar\omega_{12} = \varepsilon_2 - \varepsilon_1 = \frac{3\hbar^2 \pi^2}{2m^* L_{QW}^2}. \tag{1.2}$$

A dipole moment of a transition from the level n to m, $\langle p_{mn} \rangle$, is given by

$$\langle p_{mn} \rangle = \langle m|ez|n\rangle = \frac{8eL_{QW}}{\pi^2} \frac{mn}{(m^2 - n^2)^2}. \tag{1.3}$$

In a two-dimensional electron gas (2DEG), dipole moment associating with transitions is limited in perpendicular direction to 2DEG plane (z-direction). By using Eq. (1.1) and Eq. (1.3), oscillator strength f_{mn} , therefore, is

$$f_{mn} = \frac{2m^*(\varepsilon_m - \varepsilon_n)}{\hbar^2 e^2}\langle p_{mn}\rangle^2 = \frac{64}{\pi^2}\frac{m^2n^2}{(m^2-n^2)^3}, \tag{1.4}$$

and we have $f_{21} = 0.96$ by substituting $m = 2, n = 1$. The result suggests that the $1 \rightarrow 2$ transition dominates comparing to other intersubband transitions.

1.2.2 Photo-detection mechanism of CSIP

CSIP is a quantum-effect device implemented in a double quantum-well (QW) structure, in which the two QWs are named upper QW and lower QW here, as shown in Fig.1.4. Infrared photons are absorbed via intersubband transition in the upper QW. The excited electrons immediately tunnel out from the upper QW and escape to the lower QW due to the potential gradient. The upper QW is thereby positively charged up and the charged upper QW conduces to increase of the conductance in the lower QW. As a result, we can detect infrared photons by measuring current increase in the lower QW. A photo-active region in the upper QW is defined by negatively biasing two isolation gates (IG) and one reset gate (RG) (Fig.1.4(b)). CSIP behaves as a kind of photo-sensitive field effect transistor (FET).

In the case of conventional scheme such as photoconductors, photocurrent comes from carriers (electrons and/or holes) generated by absorptions of incident photons. Owing to this scheme, photocurrent to the incident radiation power P is expected as

$$I = \eta \frac{P}{h\nu} Ge, \tag{1.5}$$

where $h\nu$ is the incident photon energy, η is the quantum efficiency for absorption, and G is the photoconductive gain which is expected to be the order of unity for well-designed detectors. This means that the one photon absorbed in the detector produces effective charge of Ge.

For new scheme of CSIP, photo-excited electrons escape to the lower QW. The positively-charged upper QW keeps the conductivity in the lower QW higher until discharging of the upper QW, whose timescale is expected to be more than 1 second for nominal CSIP. Thanks to this scheme, CSIP detects the incident photons as the photocurrent increment. Increase of photocurrent due to single photon absorption (ΔI_e) depend on the electron mobility (μ_e) in the channel (lower QW), the channel length (L), and the channel bias (E):

$$\Delta I_e = \frac{e\mu_e E}{L} = \frac{\alpha e \mu_e V_{DS}}{L^2}, \tag{1.6}$$

here, the electric field $E = \alpha V_{DS}/L$ is used. V_{DS} is the applied voltage between drain and source electrode, and α is a geometrical factor of the device taken into account the voltage drops in the channel (usually order of unity). As a function of the number of the accumulated positive charges in the isolated upper QW island, the photocurrent through the channel increase linearly. That is, if the isolated upper QW island is charged up to Ne^+, the current through the lower QW increase $N\Delta I_e$ as a consequence. Thus, the photo-current increase in time interval t, $I_{CSIP}(t)$, is given by

$$I_{CSIP}(t) = \eta \frac{P}{h\nu} t\, \Delta I_e. \tag{1.7}$$

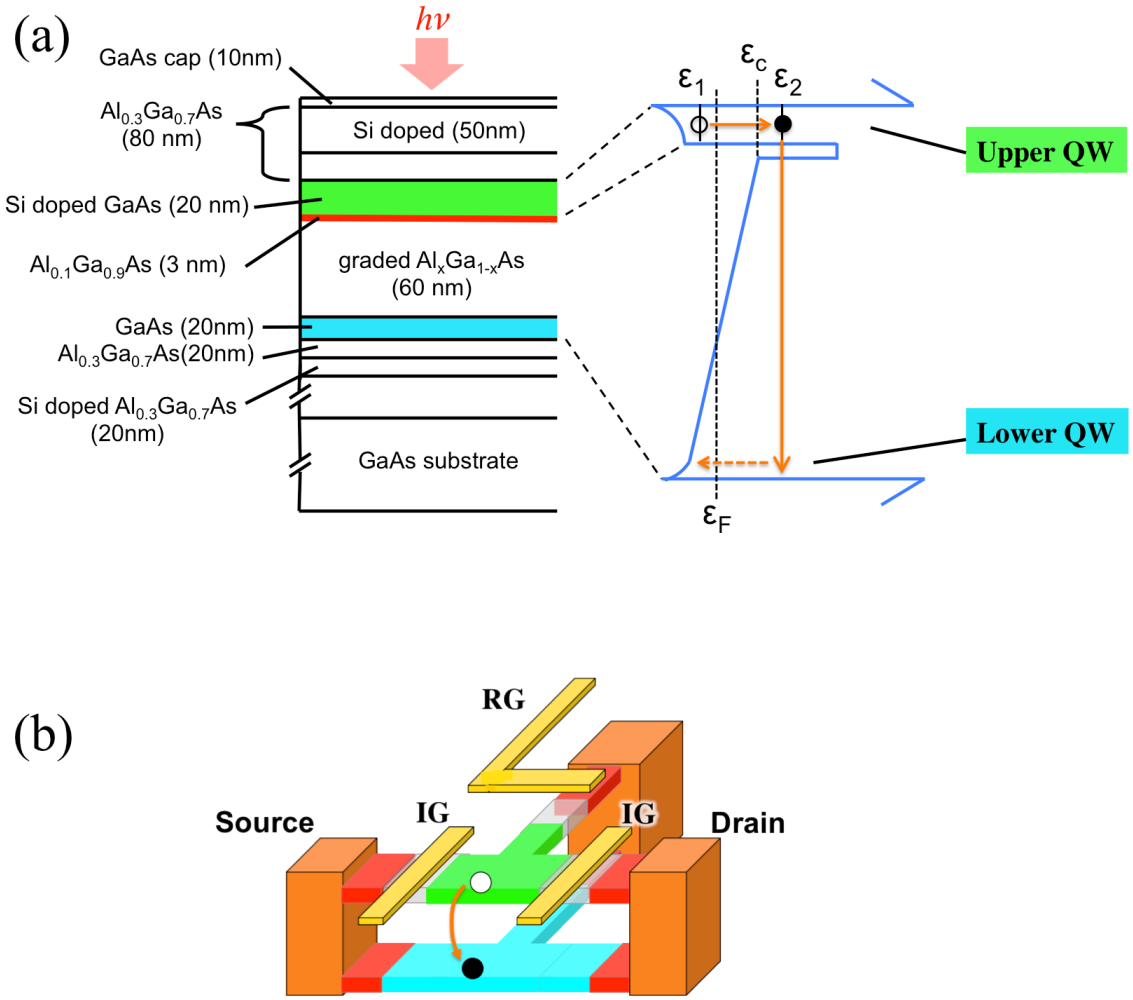

Figure 1.4: (a) CSIP crystal structure and potential diagram for the target wavelength of 48 μm as an example. The light green layer indicates the upper QW, and the light blue indicates the lower QW. The red line corresponds to the tunnel barrier. The right-hand side figure shows the potential diagram of conduction band. ε_1 and ε_2 are intersubband levels, ε_F is the Fermi energy, and ε_c is the top of the graded potential barrier. (b) Schematic representation of a CSIP device. The light green and blue layer corresponds to the wafer structures shown in (a). The upper QW is electrically isolated by applying voltage bias into Isolation gates (IGs) and the reset gate (RG). RG is also applied the voltage pulse to prevent saturation.

1.2.3 Operation of CSIP

The basic device design of CSIP is shown in Figure 1.4(b). There are two electrodes, named "drain" (D) and "source" (S) to apply the proper voltages to the device. Furthermore, there are three control electrodes, one of which is the reset gate (RG) and others are isolation gates (IGs). These three control gates are utilized to form the isolated upper QW island, which works as a photo-active region. RG is also assigned for discharge of the isolated upper QW island.

To operate the CSIP device, proper bias voltage should be applied to these electrodes. Figure 1.5 shows the drain-source current (I_{DS}) as a function of the IGs and RG voltage (V_G). The solid (red) line and the dashed (blue) line correspond to the conditions with and without the radiation. A small dip of the solid (red) curve around $V_G = -0.38$ V indicates the threshold voltage (V_{th}). Below the threshold voltage, the upper QW is electrically isolated, which works as the photo-active region.

Figure1.5 also shows the bump of the drain-source current below the threshold voltage ($V_G < -0.38$ V). This is the photo-signal indicating the accumulation of positive charge in the isolated upper QW. Therefore, IGs and RG are set to around $V_G = -0.42$ V to operate the CSIP as a photo-detector. The lower QW channel falls to disconnect with higher gate voltage bias and is fully isolated at $V_G < -1.2$ V.

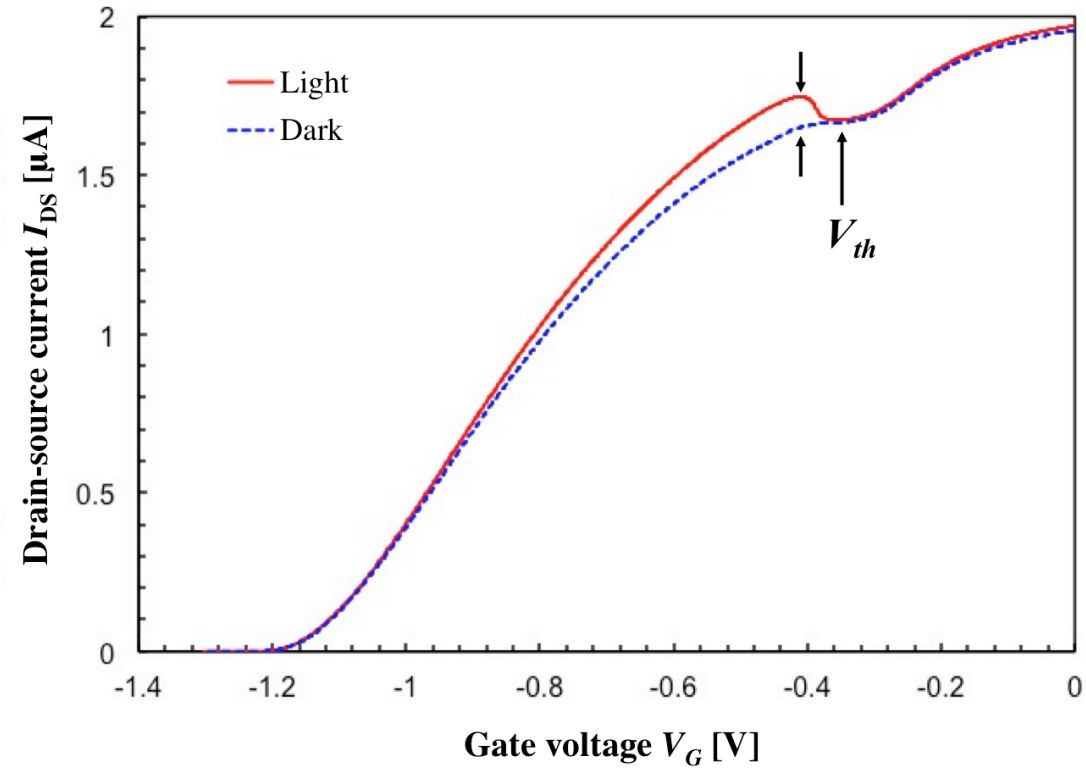

Figure 1.5: Drain-source current (I_{DS}) as a function of the IGs and RG voltage (V_G). The current I_{DS} was measured sweeping V_G between 0V and − 1.3V. The solid (red) line and the dashed (blue) line correspond to the conditions with and without the radiation. Below the threshold voltage (V_{th}), the upper QW is electrically isolated. There is the bump of I_{DS} indicated between the two vertical arrows. This bump is photo-signal due to the accumulation of positive charges in the isolated upper QW.

Since the photo-active region, i.e. isolated upper QW island, is floating electrically, positive charges generated by photon absorptions are accumulated in the upper QW. As a result of charging up in the isolated upper QW island, the potential band of the double QW changes as shown in Fig.1.6. The potential of the graded barrier is suppressed with decrease in the potential of the upper QW due to charging up. If the potential of the graded barrier is suppressed, probability of the recombination of positive charges increase. Finally, the generation and recombination rate is balanced, i.e. saturation of the photo-current.

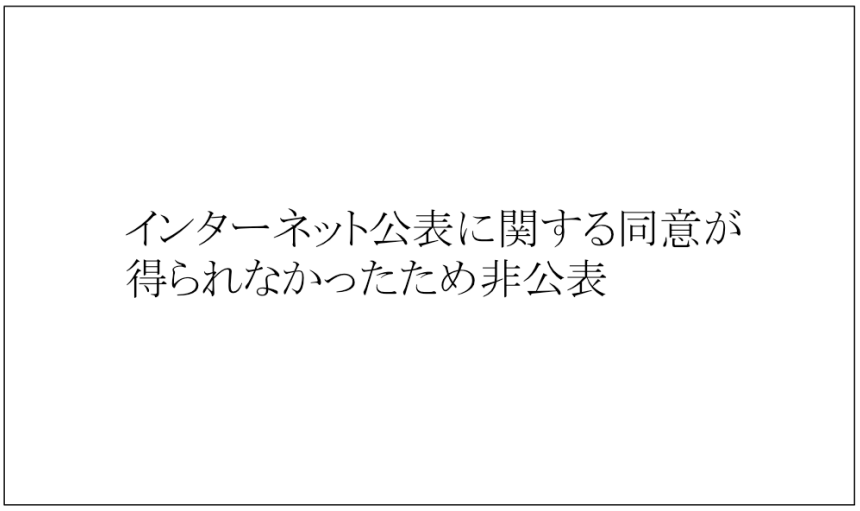

Figure 1.6: Potential diagram illustrating saturation of photo-signal [14]. (a) No deformation in initial/dark condition. (b) Moderate deformation in the linear response regime. (c) Strong deformation in the saturated regime. The drop of the electrostatic potential of the upper QW (U) increases with charge accumulation.

This situation can be seen in Fig.1.7(b). The measurements were carried at 4.2 K. This plot shows the time profile of photo-signal under the constant irradiation. The signal increases gradually from the zero photo-signal which correspond to the discharge of the upper QW. A slope of the photo-signal, however, becomes moderate with accumulation of charges and flats finally. Therefore, the discharge operation of the upper QW should be required for continuous operation of CSIP. To discharge the upper QW, RG is applicable. Applying the short pulse to RG, CSIP can operate continuously as shown in Fig.1.7(a). The interval of the discharge operation should be selected within the linear region of the photo-response, where the recombination of the escaped electron is negligible.

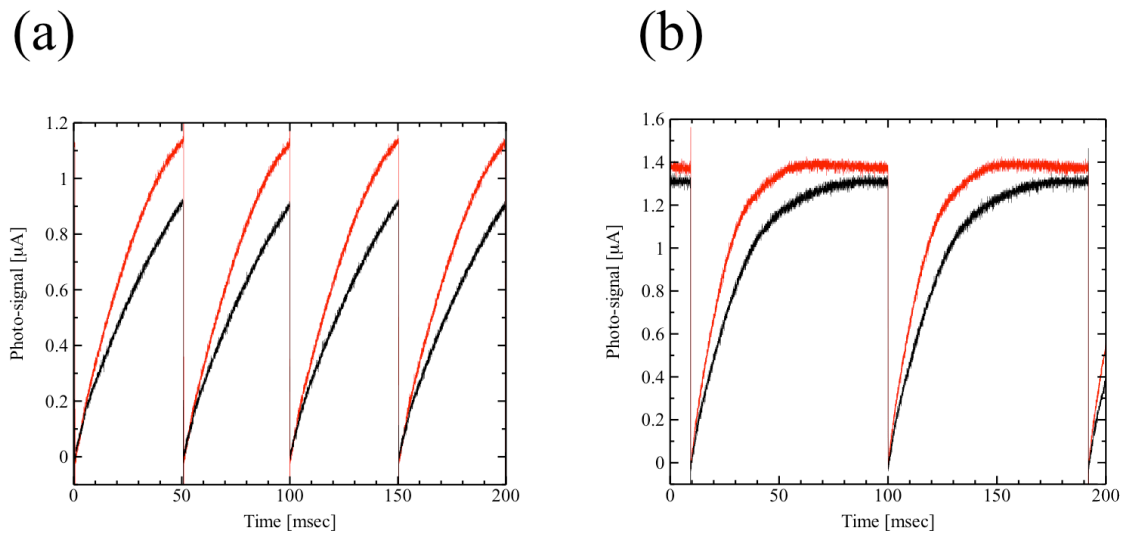

Figure 1.7: Time trace of photo-signals at $V_G = -0.41$V at the reset repetition rates of 40Hz (a) and 11Hz (b). Different incident radiation intensities are indicated by red (higher intensity) and black (lower one). Photo-signal is saturated in (b). The measurements were carried at 4.2K.

Averaged photo-current within a reset interval is given as

$$I_{CSIP} = \eta \frac{P}{h\nu} \frac{\tau_{\text{reset}}}{2} \Delta I_e. \tag{1.8}$$

where τ_{reset} is the reset interval. This is a modification of Eq.(1.7) for actual condition. If we compare Eq. (1.8) with Eq. (1.5), corresponding photoconductive gain (G_{CSIP}) can be written by

$$G_{\text{CSIP}} = \frac{\tau_{\text{reset}}}{2e} \Delta I_e. \tag{1.9}$$

From Eq.(1.6) and Eq.(1.9), we obtain $G_{\text{CSIP}} \sim 2 \times 10^5$ assuming $\tau_{\text{reset}} = 100$ms, $L = 300\mu$m, $\mu_e = 10^4$ cm^{2}V^{-1}s^{-1}, and $V_{DS} = 10$mV as typical parameters of CSIPs we developed. This huge value of photoconductive gain gives CSIP ultra-highly sensitivity.

When considering the natural background limited performance, observing performance is restricted by photon statics. The quantum efficiency η is the dominant parameter in this case. For the fundamental reason, the quantum efficiency of CSIP is constrained to smaller than that of conventional semiconductor devices. CSIP has the photo-sensitive upper QW layer just below the surface (about 100 nm-width). In a two-dimensional electron gas (2DEG) layer, dipole moment associating with transitions is limited in perpendicular direction to 2DEG plane (z-direction). CSIP requires photo-coupling antenna that transforms the horizontal electric fields of incident radiation into the vertical oscillating electric fields in the upper QW right below the antenna itself. Cross-hole antenna arrays used in this paper have achieved the quantum efficiency of 7% [15].

1.2.4 Other characteristics

CSIP has ultra-high sensitivity due to the amplification mechanism of photo-electrons. In addition to the excellent sensitivity, CSIP is featured by a number of merits, such as a huge dynamic range (> 10^6 by choosing proper reset interval) and low output impedance (10^3-10^4 Ω) [1]. CSIP can work very well at the nominal cryogenic temperature [12] in comparison to the high sensitive

transition edge sensor (TES) bolometers which require sub-K temperature. Actually, the performance of CSIP has temperature dependency through the increase of the recombination rate by thermal-activated electrons. One of the excellent features of CSIP is that the target wavelength can be designed by properly choosing the width of the upper QW. As seen in Fig.1.8, photo-signal has finite spectral bandwidth that depends on interface roughness [16], lattice scattering [17], and escape probability of electrons from the upper QW [12][18].

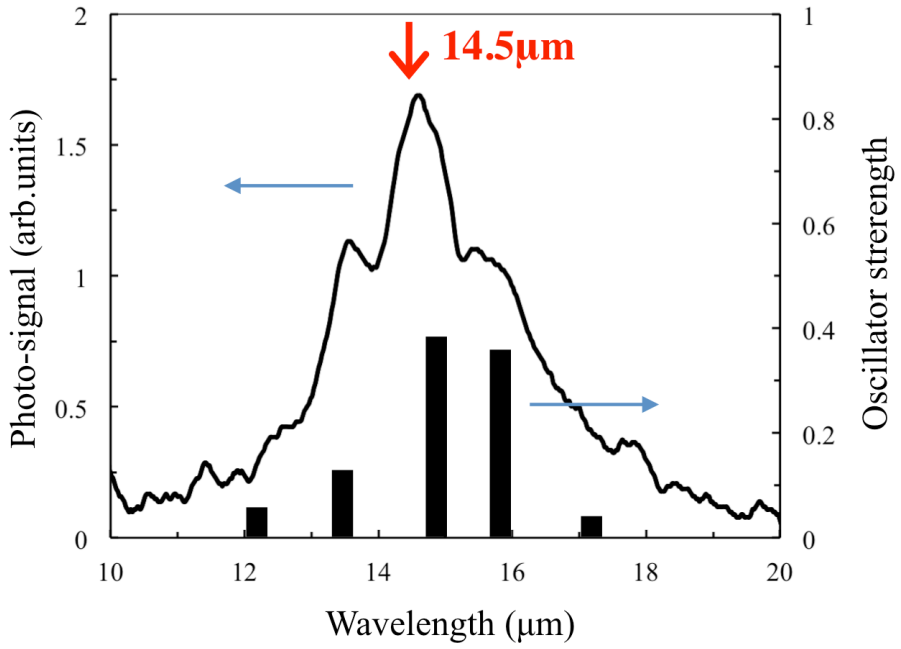

Figure 1.8: Photo-response spectrum of 15 μm CSIP [S. Kim et al., submitted]. The value of 14.5 μm is the designed wavelength taken into account Depolarization shift. The figure also shows the wavelengths corresponding to the simulated transitions with relevant oscillator strengths as discussed below.

Chapter 2

Photo-response in the Vicinity of Reststrahlen Band

2.1 Background

The aim of this work is to achieve better understanding of the photo-response of CSIP in a longer-wavelength range (30 – 60 μm): Particular motivation behind this is to develop ultra-highly sensitive CSIPs applicable to astronomical purposes. In general, when we aim at expanding the wavelength range in the infrared region utilizing III-V compound semiconductors, we have to pay special attention to the so called "Reststrahlen band", which is defined by the Longitudinal Optical (LO) phonon frequency, ω_{LO}, and the Transverse Optical (TO) phonon frequency, ω_{TO}. In GaAs (ω_{LO} = 36.7 meV, ω_{TO} = 33.7 meV), the Reststrahlen band is located in the range between 33.8 μm (LO) and 36.8 μm (TO) at 4K [19] [*1]. As shown in Fig.2.1(a) the light in Reststrahlen band is strongly reflected and absorbed, due to strong coupling of photons with TO phonons [21]. Since the light does not penetrate substantially into the material, photo-response is completely absent in the Reststrahlen band, as exemplified for quantum-well infrared photodetectors (QWIP) in Fig.2.1(b) [21]. This fact has been well established both experimentally and theoretically in all other conventional detectors based on III-V compound semiconductors.

In CSIP, however, the situation is largely different: Reststrahlen band provides us with a new and extremely interesting subject of photo-response study. This is because the photo-active region in CSIP is strictly limited to the upper quantum well (QW) that is located immediately below the surface (about 100 nm depth). The photo-active region is well within the penetration depth of the radiation in Reststrahlen band (around a few microns). Hence, CSIPs are expected to exhibit finite response to the radiation in Reststrahlen band: Moreover, the response will be of particular interest because of strong interaction of electrons with LO phonons (Polaron effect) and strong interaction of photons with TO phonons (Polariton effect). It will be important to experimentally clarify how these interactions play their roles in the photo-response mechanism. For this sake, we have designed and fabricated CSIPs especially for the Reststrahlen band in this work; viz., upper QW width along with the overall crystal structure were so designed that the target wavelength falls in the Reststrahlen band. In the following sections, sample preparation is described, and unexpected new experimental results are presented.

[*1] In GaN and InP crystals, the Reststrahlen bands lie in 14 – 18 μm [20] and 29 – 33 μm [19], respectively. In order to avoid the Reststrahlen band of GaAs, we could choose these materials. However, GaAs systems are the most well known/developed materials for quantum-well detectors. So, we limit our investigation to GaAs/AlGaAs crystals.

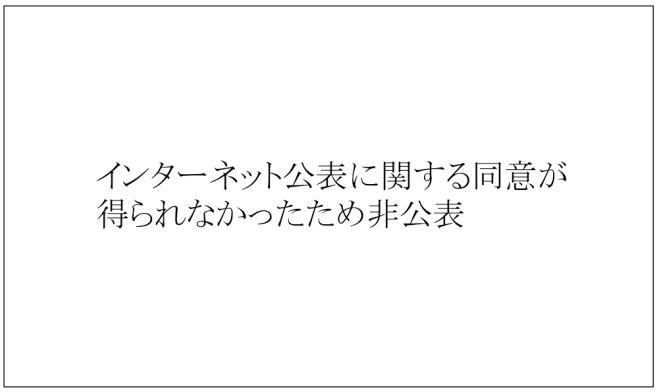

Figure 2.1: Characteristics of QWIP [21]. (a) The real refractive index and the extinction coefficient for GaAs at 8K in a spectral range including the Reststrahlen band. (b) Calculated and experimental photo-response spectrum. The QWIP device studied consists of 50 quantum-wells of 12 nm-thick GaAs layers separated by 40 nm-thick $Al_{0.05}Ga_{0.95}As$ layers.

2.2 Experimental Methods

2.2.1 GaAs/AlGaAs double quantum well structure

We studied three crystals of GaAs/AlGaAs double quantum well shown in Figs. 2.2 (a), (b) and (c). The target wavelengths of the crystals, which we designate as DQW-32, DQW-36, and DQW-48, are designed to be 32, 36 and 48 μm, respectively, as indicated in Table 2.1. The method of design is described later.

The band structure of CSIP has to satisfy the following conditions, which are more demanding for longer target wavelengths (since relevant photon energies are smaller). In the upper QW, electrons are in the ground state (energy ε_1) under the absence of photons. When photons are absorbed, electrons are excited to the first excited state (ε_2) and rapidly tunnel out of the QW. These requirements are represented by the conditions (Fig.1.4(a))

$$\varepsilon_1 < \varepsilon_F < \varepsilon_c < \varepsilon_2, \tag{2.1}$$

where ε_F is the Fermi energy and ε_c is the top of the graded potential barrier. Here,

$$\varepsilon_c - \varepsilon_F \gg k_B T \tag{2.2}$$

(k_B: Boltzmann constant $1.38 \times 10^{-23}\mathrm{JK}^{-1}$, T: temperature) is necessary to assure long recombination lifetime of the photo-holes in the upper QW ($k_B T$ = 0.36 meV at 4.2K). The relevant parameter to ε_F is the two-dimensional electron density (N_{2DEG}) of the upper QW,

$$N_{2DEG} = \frac{m^*}{\pi\hbar^2}\left(\varepsilon_F - \varepsilon_1\right), \tag{2.3}$$

where m^* is the effective mass in GaAs (m^*=0.067m_e with the free electron mass m_e). In addition, it is desirable from Eq. (1.6) that the electron mobility of the lower QW (μ_L) is as high as possible, so that the signal current amplitude by one electron (ΔI_e) is large. The electron density in the lower QW (n_L) should be minimized in order to suppress the background dark current or shot noise. The Si–doping level for the upper QW is designed for the electron density in the upper QW

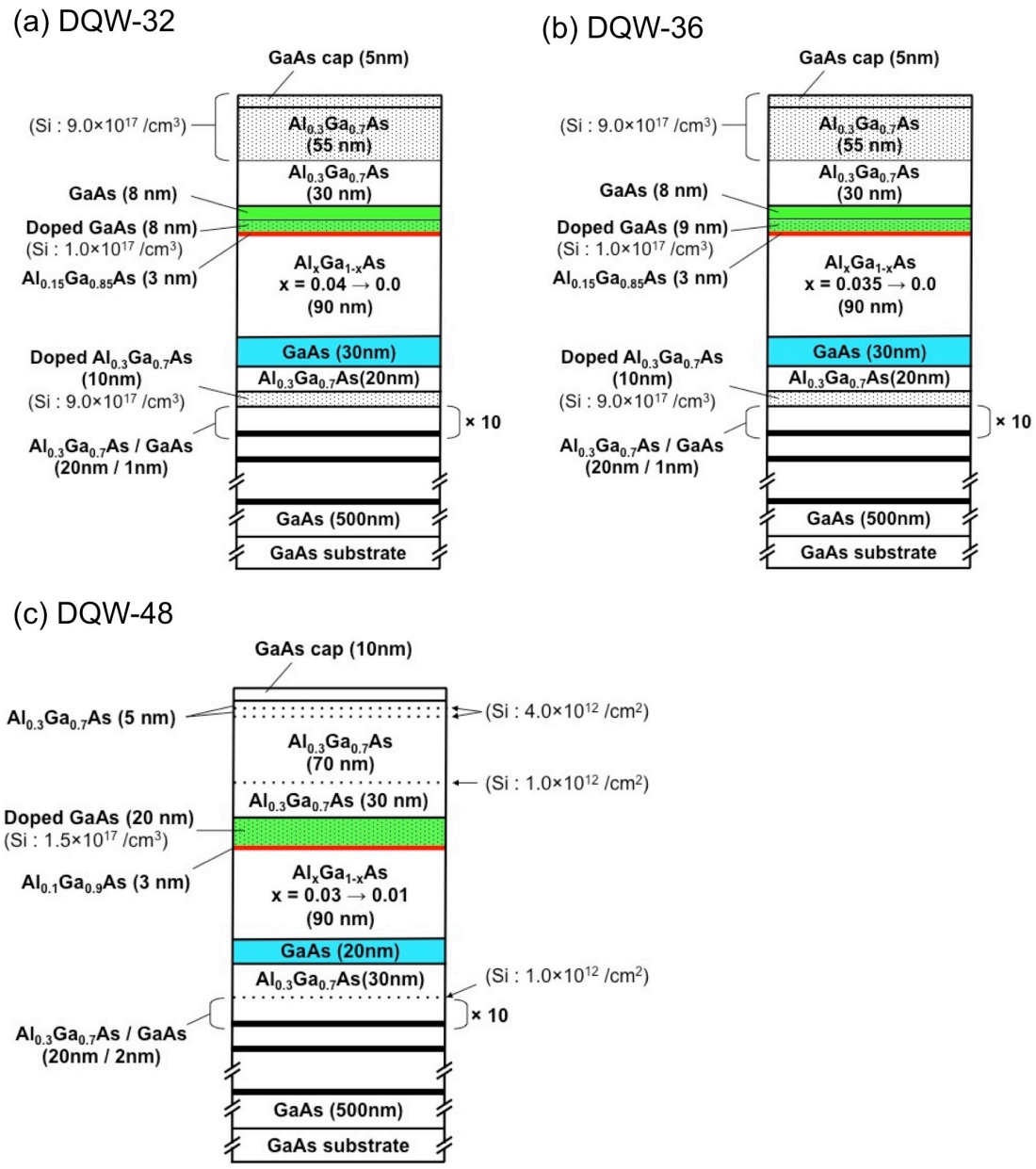

Figure 2.2: CSIP crystal structure for (a) DQW-32, (b) DQW-36, (c) DQW-48. The light green layer indicates the upper QW, and the light blue indicates the lower QW. The red line corresponds to the tunnel barrier. The dotted area and the dotted lines are Si-doped and Si delta-doped regions, respectively.

to be $n_U = 2.5 \times 10^{11}\mathrm{cm}^{-2}$ (corresponding to $\varepsilon_F - \varepsilon_1 = 10$ meV) by using Eq.(2.3). The design parameters and the specifications of the crystals are summarized in Tables 2.1 and 2.2.

The target wavelengths (the transition energies) are derived through a simulator "*nextnano3*", which solves one-particle Schrödinger equation and Poisson equation self-consistently for given values of band parameters. The true experimental parameter values realized in actual crystals can be slightly different from the designed values. The true structure parameters were investigated through Secondary Ion Mass Spectrometry (SIMS) method, as Fig.2.3 displays an example for DQW-32. In this example, we can notice that the aluminum content in the barrier layer is x = 0.34 whereas the designed value is x = 0.30 and Si-doping concentration is slightly different from the designed value. Nevertheless, we confirmed for the three crystals that the basic crystal structure is firmly formed with sufficiently low level of impurity contamination.

Simulation (*nextnano3*) was carried out by using parameter values determined through the SIMS inspection. Figures. 2.4 through 2.6 display the wave functions with the five largest oscillator strengths for the three crystals, respectively. All the possible transition energies are derived along with relevant oscillator strengths. In Fig.2.4 through 2.6, there are multiple excited levels with finite oscillator strengths from the ground level. These excited levels are attributed to the interference of the electron wave function (ε_2) extending in the whole region including the upper QW, the graded barrier region and the lower QW (The upper QW is not isolated but is coupled through tunneling with its larger neighboring region reaching the lower QW.) The wavelength obtained from the oscillator strength-weighted average of the multiple transition energies, $\langle\varepsilon_{12}\rangle$, is defined to be the "average wavelength $\langle\varepsilon_{12}\rangle$", and is listed in Table. 2.1. It is noted that the average wavelengths $\langle\varepsilon_{12}\rangle$ are slightly different form the target wavelengths (designed) but the difference is small.

Table 2.1: CSIP structure parameters for the upper QW.

Sample name	Wavelength		Upper QW (GaAs)			
	Target	$\langle\varepsilon_{12}\rangle$ *1	Well width	Si-well doping	n_U *2	μ_U *2
	[μm]	[μm]	[nm]	[$10^{17}\mathrm{cm}^{-3}$]	[$10^{11}\mathrm{cm}^{-2}$]	[$10^4\mathrm{cm}^2$/V s]
DQW-32	32	32.2	16	1.0	2.6	12
DQW-36	36	35.7	17	1.0	2.5	16
DQW-48	48	48.6	20	1.5	2.4	3.8

*1 The wavelength defined from the oscillator strength-weighted average of the multiple transition energies, $\langle\varepsilon_{12}\rangle$.

*2 (n_U, μ_U) is (the electron density, the electron mobility) of the upper QW.

Table 2.2: CSIP structure parameters for the barrier layers and the lower QW.

Sample name	Tunnel barrier x *1	Graded barrier x *1	Lower QW (GaAs) Well width [nm]	n_L *2 [10^{11}cm^{-2}]	μ_L *2 [10^4cm^2/V s]
DQW-32	0.15	0→0.04	30	3.2	4.4
DQW-36	0.15	0→0.035	30	3.2	7.4
DQW-48	0.1	0.01→0.03	20	4.0	19

*1 Aluminum composition of $Al_xGa_{1-x}As$. Tunnel barrier width is designed to be 3nm for all samples.

*2 (n_L, μ_L) is (the electron density, the electron mobility) of the lower QW.

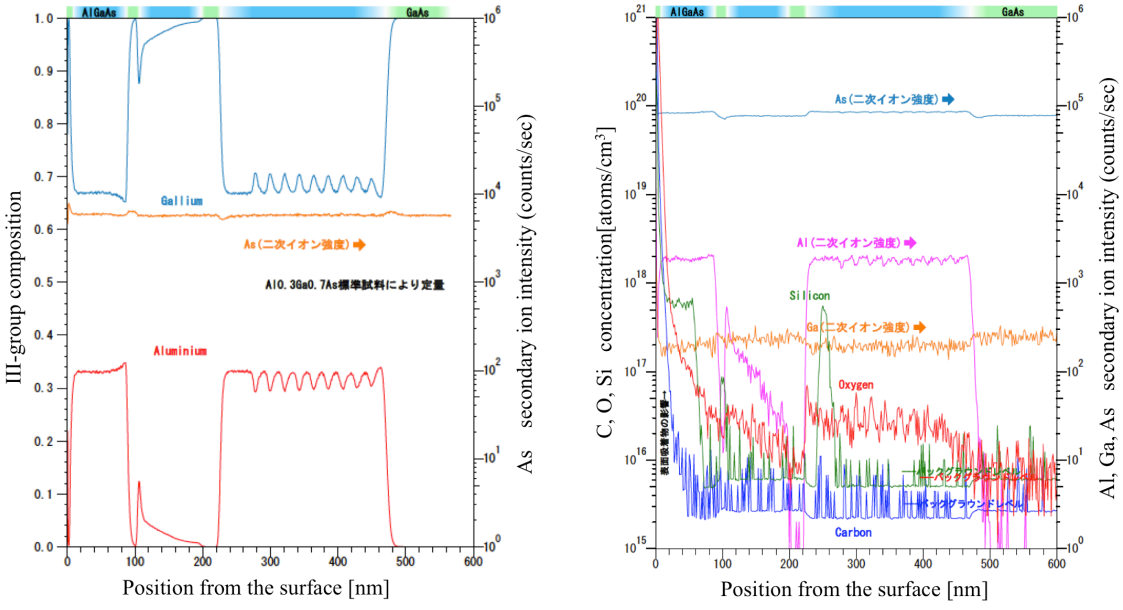

Figure 2.3: SIMS data for DQW-32. The left-hand figure shows the depth profile for Ga (blue) and Al (red) composition with secondary ion intensity [counts/sec] for As (yellow). The right-hand figure shows the depth profiles for C (blue), O (red), and Si (green) concentration [atoms/cm^3] with secondary ion intensity [counts/sec] for Ga (yellow), Al (pink), and As (light blue).

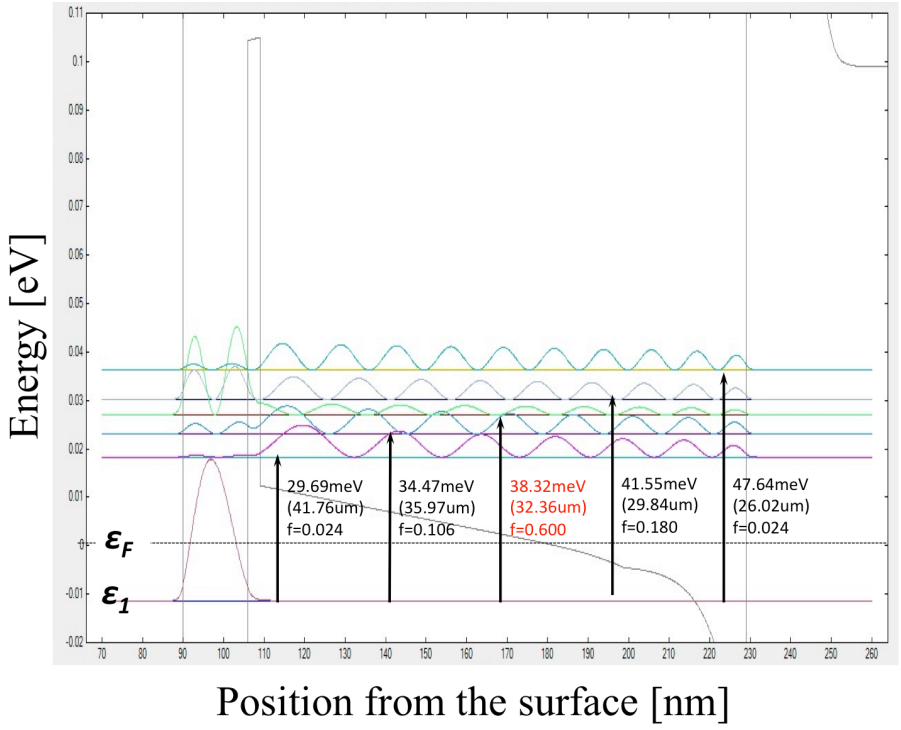

Figure 2.4: Calculated wave functions for DQW-32 using *"nextnano3"* simulator. The simulation were taken into account the wafer structure measured by SIMS. ε_F is defined as zero point in the simulator. This shows the wave functions with the five largest oscillator strengths and each transition energy from the ground state.

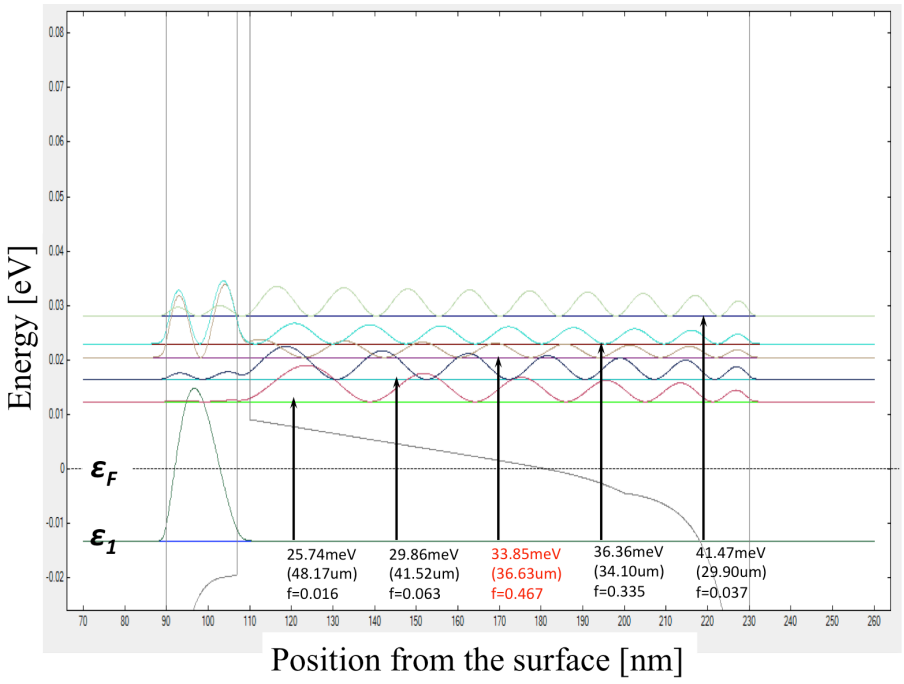

Figure 2.5: Calculated wave functions for DQW-36 using *"nextnano3"* simulator. The simulation were taken into account the wafer structure measured by SIMS. ε_F is defined as zero point in the simulator. This shows the wave functions with the five largest oscillator strengths and each transition energy from the ground state.

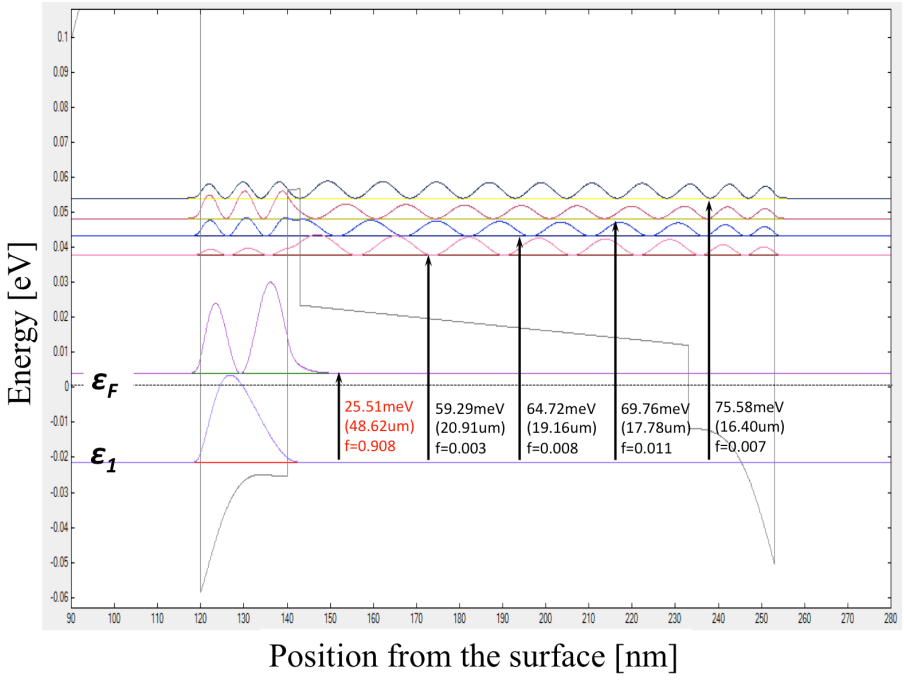

Figure 2.6: Calculated wave functions for DQW-48 using *"nextnano3"* simulator. The simulation were taken into account the wafer structure measured by SIMS. ε_F is defined as zero point in the simulator. This shows the wave functions with the five largest oscillator strengths and each transition energy from the ground state.

2.2.2 Device structure

Devices in this study (Fig.2.7) were fabricated through Electron Beam Lithography (EBL). A bilayer 2DEG channel (the upper and the lower QW) of 100 μm-width and 350 μm-length is defined by wet mesa etching (90 nm-depth for DQW-32 and DQW-36, and 100 nm-depth for DQW-48). Ohmic contacts to the both 2DEG layers are formed by alloying with a 200-nm-thick AuGe/Ni layer. The four Isolation gates (IG) and three coupler gate (CG) are formed by depositing a 20nm/80nm-thick NiCr/Au layer.

As elucidated in Fig.2.8, cross-hole metal mesh deposited on top of the channel serves as an antenna or a photo-coupler. Earlier work on a 15 μm CSIP [15] demonstrated that this type of coupler yields a quantum efficiency around 7%. The sensitivity takes a maximum when photo-coupler period, p, is nearly equal to the wavelength in GaAs. The dielectric constant of GaAs largely vary in the Reststrahlen band according to

$$\epsilon(\lambda) = \epsilon(\infty)\left(\frac{\lambda^2 - \lambda_{LO}^2}{\lambda^2 - \lambda_{TO}^2}\right). \tag{2.4}$$

Hence the real part of refractive index n(λ) (= $\sqrt{\epsilon(\lambda)}$) largely varies accordingly. Nevertheless, the relation between p and λ_n remains in the wavelength range longer than 15 μm [22]. For the devices in this work, cross-hole antennas with six different periods spanning from 6.0 to 22.3 μm are formed on single device as shown in Fig.2.7 in order to assure reasonable sensitivity in the Reststrahlen band. More detailed parameters of the photo-coupler are summarized in Table 2.3.

Table 2.3: The photo-coupler periods used in this work

Photo-coupler	Period [μm]
C1	6.0
C2	7.8
C3	10.1
C4	13.2
C5	17.1
C6	22.3

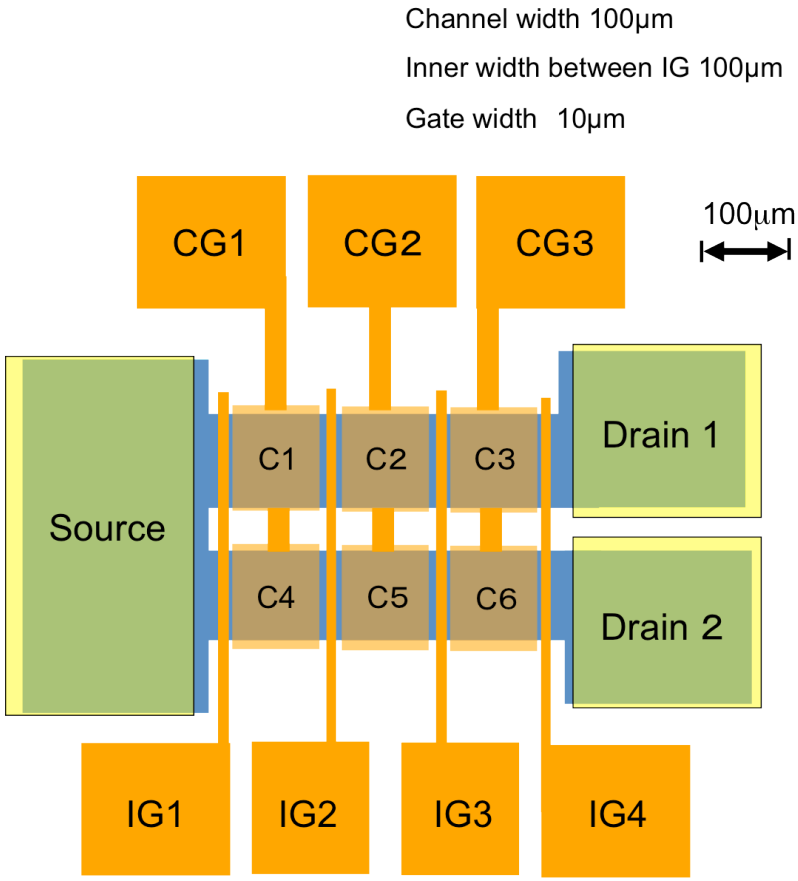

Figure 2.7: The design pattern of devices. The blue area is defined by wet mesa etching. Ohmic contacts to the double QW layer are indicated by the yellow areas. The metal gates and the photo-couplers (orange areas) are formed by depositing a 20nm/80nm-thick NiCr/Au layer.

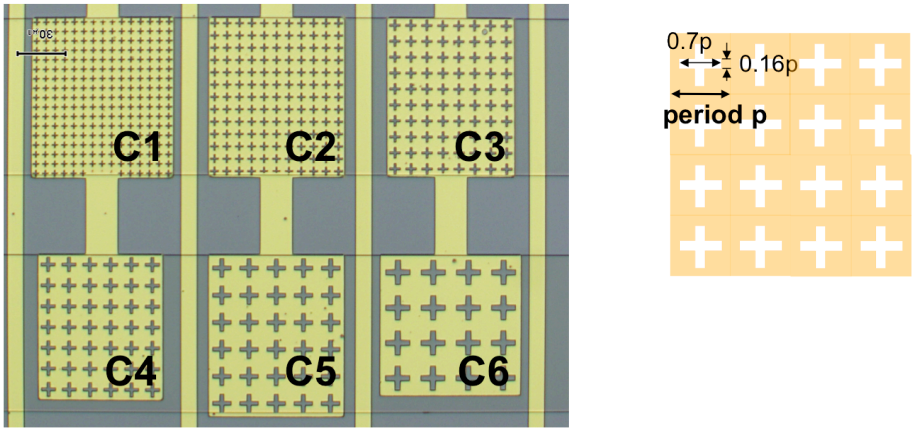

Figure 2.8: (a) The micrograph of the photo-couplers. The photo-couplers (C1 to C6) are designed with different cross-hole period p indicated in (b). (b) The photo-coupler design. The cross-hole antennas are arranged with a constant period p. The length and the width of the cross-holes are fixed to 0.7p and 0.16p. The values of p used in this work are listed in Table 2.3.

2.2.3 Experimental set up

Throughout this work, experimental results obtained from CSIP devices fabricated in three different wafers, DQW-32, DQW-36 and DQW-48, are described. All the experiments were carried at liquid Helium temperature (4.2K). The devices are irradiated by the monochromatic light generated by monochromator (CT–25) at room temperature through the light pipe as shown in Fig. 2.9. The monochromator covers the spectral ranges from 20 μm through 54 μm, by using three diffraction gratings (with Blaze wavelength being 30, 36 and 45 μm). The light transmitted through the monochromator is modulated by a chopper inside the monochromator at a frequency from 6Hz to 100Hz (Table 2.4). The spectrum of the transmitted light was calibrated by using a pyroelectric detector and filters. Additional parameters adopted in the measurements are listed in Table 2.4.

One of the isolation gate (IG) is used also as a reset gate (RG). Six different antennas are selectable by appropriately biasing IGs, so that spectral response of each photo-coupler antenna can be separately studied.

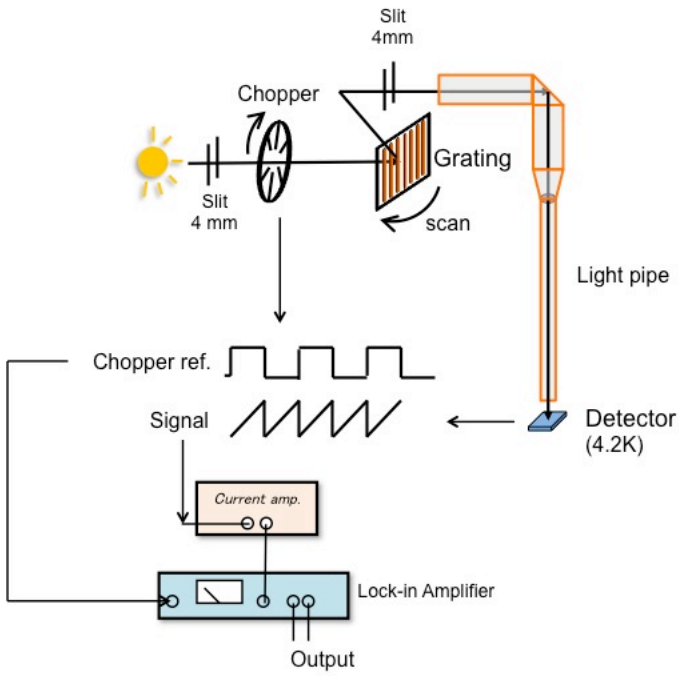

Figure 2.9: Setup for Spectral Measurement.

Table 2.4: Operation parameters of test devices for the spectral measurements.

Experimental parameter	DQW-32	DQW-36	DQW-48
Isolation gate bias	− 0.41V	− 0.42V	− 0.57V
Reset gate pulse voltage	+0.30V	+0.15V	+0.40V
Reset gate pulse width	2μsec	2μsec	2μsec
Chopping frequency	10Hz	100Hz	6Hz
Blaze wavelength of grating	36μm	36μm	45μm
Grating scan speed	48nm/sec	48nm/sec	60nm/sec
Time constant	1sec	1sec	1sec

2.3 Experimental Results

2.3.1 Spectral photo-response

Spectral photo-response is displayed in Figs.2.10 through 2.14 for DQW-32, -36, -48. These photo-response was observed in the two spectral region away from the target wavelength, which has never been seen in 15 μm CSIP (Fig.1.8). Different photo-response spectra are shown separately in Figs. 2.10 (DQW-32) and 2.11 (DQW-36) for individual photo-couplers. In the measurements, each photo-coupler (C1 to C6 in Figs. 2.7 and 2.8) is selectively used by biasing appropriate isolation gates along with the choice of drain. In Figs. 2.10 and 2.11, two features are noted; viz, (i) a large response band is located around 27 μm (upper frequency branch, ω_+) and another smaller one around 34 μm (lower frequency branch, ω_-), and (ii) the longer-wavelength band, or ω_- branch, overlaps significantly the Reststrahlen band. This general features are commonly noted in all the different photo-couplers. Relative signal intensity depends on the photo-couplers but the wavelength position of relatively sharp response peaks are kept unchanged.

Individual sharp peaks noted in the response band around 27 μm (ω_+ branch) are caused by the interference of the electron wave function (ε_2) extending in the confined region from the upper QW to the lower QW as seen in Figs. 2.4 through 2.6. The feature of the spectral peaks has been observed in 15 μm CSIP (Fig.1.8), which is consistent with the feature derived from the *nextnano3*-simulated transitions with the relevant oscillator strengths. In this work, intrinsic properties of the photo-response bands should be studied rather than the coupler-specific features or the individual sharp response peaks. Hence photo-response obtained by adding all the contributions from six photo-couplers is of crucial interest. Figures 2.12, 2.13, and 2.14 show photo-response spectra obtained by biasing IG1 and IG4 with $V_{S-D1} = V_{S-D2} = 10$mV, to which all the couplers contribute nearly equally. Surprisingly, distinct photo-response is observed in the Reststrahlen band, which has never been seen in conventional QW photodetectors like QWIP [21].

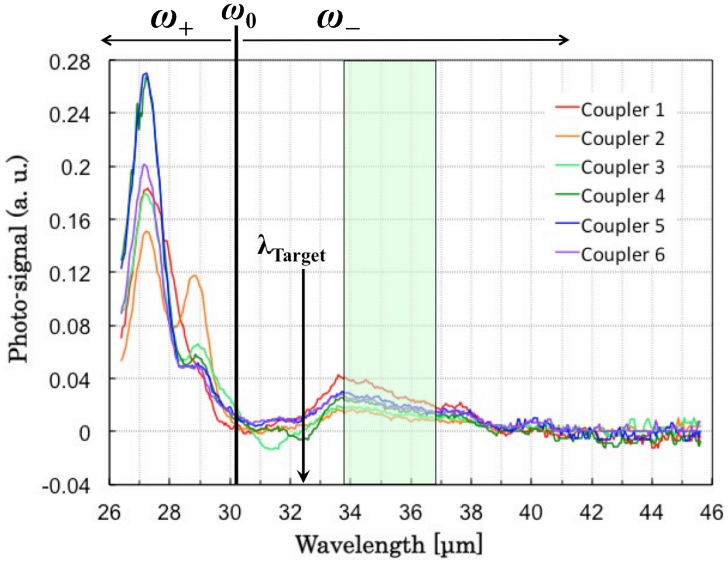

Figure 2.10: Photo-response spectra for DQW-32 with photo-couplers, C1 to C6. Each color line shows photo-response using each photo-coupler as indicated in the figure. The y-axis (a.u.) preserves relative scale of signal intensities. The shaded area is the Reststrahlen band of GaAs. The arrows indicates the target wavelength (λ_{Target}) of the measured sample. Photo-responses are split into two spectral bands (ω_+ and ω_-), which are divided at the wavelength corresponding to $\omega_0 = \sqrt{\omega_{12}^2 + \omega_P^2}$.

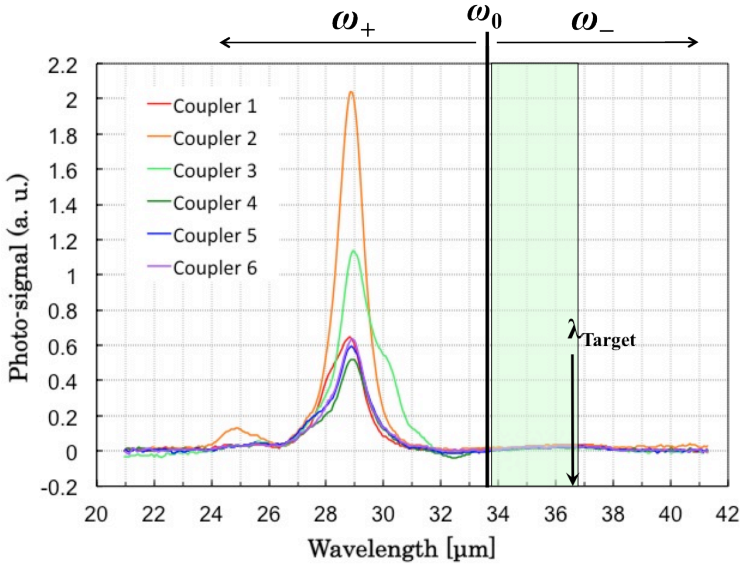

Figure 2.11: Photo-response spectra for DQW-36 with photo-couplers, C1 to C6. Each color line shows photo-response using each photo-coupler as indicated in the figure. The y-axis (a.u.) preserves relative scale of signal intensities. The shaded area is the Reststrahlen band of GaAs. The arrows indicates the target wavelength (λ_{Target}) of the measured sample. Photo-responses are split into two spectral bands (ω_+ and ω_-), which are divided at the wavelength corresponding to $\omega_0 = \sqrt{\omega_{12}^2 + \omega_P^2}$.

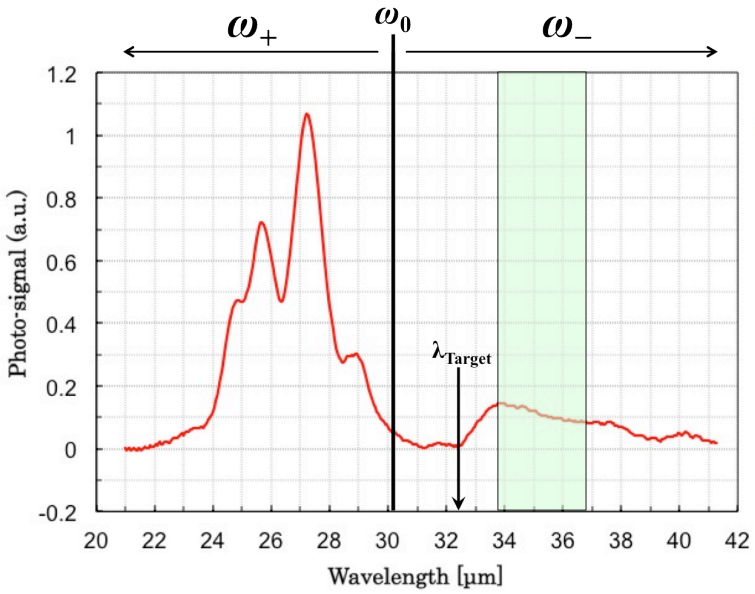

Figure 2.12: Photo-response spectrum for DQW-32. The photo-response spectrum was obtained by biasing IG1 and IG4 with $V_{S-D1} = V_{S-D2} = 10$ mV. The shaded area is the Reststrahlen band of GaAs. The arrows indicates the target wavelength (λ_{Target}) of the measured sample. Photo-responses are split into two spectral bands (ω_+ and ω_-), which are divided at the wavelength corresponding to $\omega_0 = \sqrt{\omega_{12}^2 + \omega_P^2}$.

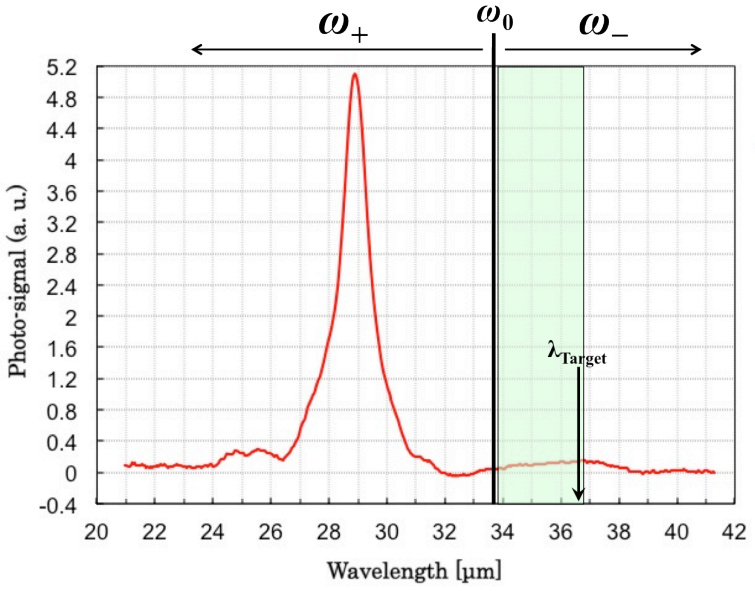

Figure 2.13: Photo-response spectrum for DQW-36. The photo-response spectrum was obtained by biasing IG1 and IG4 with $V_{S-D1} = V_{S-D2} = 10$ mV. The shaded area is the Reststrahlen band of GaAs. The arrows indicates the target wavelength (λ_{Target}) of the measured sample. Photo-responses are split into two spectral bands (ω_+ and ω_-), which are divided at the wavelength corresponding to $\omega_0 = \sqrt{\omega_{12}^2 + \omega_P^2}$.

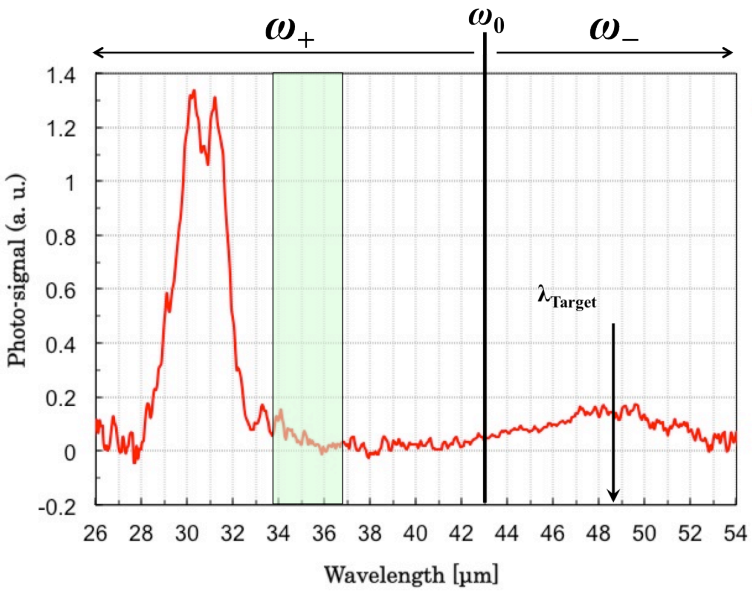

Figure 2.14: Photo-response spectrum for DQW-48. The photo-response spectrum was obtained by biasing IG1 and IG4 with $V_{S-D1} = V_{S-D2} = 10$ mV. The shaded area is the Reststrahlen band of GaAs. The arrows indicates the target wavelength (λ_{Target}) of the measured sample. Photo-responses are split into two spectral bands (ω_+ and ω_-), which are divided at the wavelength corresponding to $\omega_0 = \sqrt{\omega_{12}^2 + \omega_P^2}$.

2.3.2 Sensitivity estimation

Sensitivity can be roughly estimated from time-trace of photo-signal similar to Fig.1.7. From Eq. (A.5), NEP is lower than 4×10^{-16} W/$\sqrt{\text{Hz}}$ for the measurement of DQW-36, which gives P ~ 30pW, S/N ~ 10^2 and Δf ~ 500kHz. Because of the same experimental setup as the measurement in Appendix, the incident radiation power, P, was evaluated from Eq. (A.2) through (A.4) as λ = 29μm and $\Delta\lambda$ = 2μm. No doubt a substantially lower sensitivity (NEP < 1×10^{-18} W/$\sqrt{\text{Hz}}$ will be achieved if detector size is decreased to that of the 15 μm CSIP device (L × W = 16 × 4 μm^2) through NEP $\propto W^{1/2} \times L^{3/2}$ relation derived from Eq. (A.5). On the other hand, Transition Edge Sensor (TES) bolometers for 34–60 μm have reached NEP = 4×10^{-19} W/$\sqrt{\text{Hz}}$ [23]. TES bolometers, however, have too small current responsivity (~10^{-3}) and require extremely-low operation temperature (~100mK). Compared to TES bolometers, CSIPs have distinct advantage of easy-to-use due to outstanding current responsivity (10^{5-12}) and operation temperature (4.2K).

Chapter 3

Discussion and Interpretation

Two experimental findings described in Chapter 2,

(i) photo-response being split into two separated spectral bands and

(ii) one of the spectral bands being in (or close to) the Reststrahlen band,

cannot be explained in terms of a single-particle model of electrons. As shown in Figs.2.4–2.6, simulations (*nextnano3*) of one-particle eigenstates in the double QWs predict only one detection band around the target wavelength. In this chapter interaction of electrons with LO phonons is argued to lead to level anti-crossing, which provides reasonable interpretation of the experimental findings.

3.1 Anti-crossing due to Electron−LO Phonon Interaction

Conduction electrons in GaAs strongly interact with longitudinal optical (LO) phonons through Coulomb interaction [24]. Due to the interaction, an electron excited to the first-excited subband in the upper QW will rapidly emit one LO phonon if a photon with the energy equal to the LO phonon energy ε_{LO}, is absorbed. The electron, thereby returning to the ground subband, re-absorbs the LO phonon, and in turn, repeats coherent process of virtual emission and absorption of LO phonons.

This process leads to the formation of hybridized polaron state, which can be described explicitly by letting $|\,\mathrm{e}, 0_{LO}\rangle$ be the ket vector of the state with an electron in the excited subband and zero LO phonon, and $|\,\mathrm{g}, 1_{LO}\rangle$ be that of the state with the electron in the ground subband and one LO phonon. The eigenvector is expressed by a superposition of the two states,

$$|\pm\rangle = \mathrm{A}^{\pm}\,|\,e, 0_{LO}\rangle + \mathrm{B}^{\pm}\,|\,g, 1_{LO}\rangle, \tag{3.1}$$

where $\mathrm{A}^{\pm}$ and $\mathrm{B}^{\pm}$ are appropriate complex numbers. As schematically shown in Fig.3.1, eigenenergies of the upper and the lower branches show level anti-crossing as the intersubband energy difference, ε_{12}, is scanned across the LO phonon energy, ε_{LO}. Fundamental quantum mechanics predicts that the amplitude of energy splitting at $\varepsilon_{12} = \varepsilon_{LO}$ is 2W, where W ≈ 2 meV (GaAs) is the electron-LO phonon interaction energy [25][26].

The scenario of anti-crossing described in the above is justified only when the electron/phonon system is in a quantum-mechanically undisturbed state to assure coherent interaction between electrons and LO phonons. This condition is satisfied in the present system because (i) the lifetime of the excited electron state is evaluated from the spectral line width (FWHM ≈ 1.2 μm) to be ca. 4 psec, which is longer than the electron-LO phonon interaction time $\hbar$/W ≈ 1.5 psec and (ii) the lifetime of LO phonons (ca. 7 psec [27]) is also longer than $\hbar$/W ≈ 1.5 psec.

It is hence highly probable that the intersubband transition in CSIP coherently couples with LO phonons. The experimentally observed amplitude of energy splitting is ca. 10 meV, which

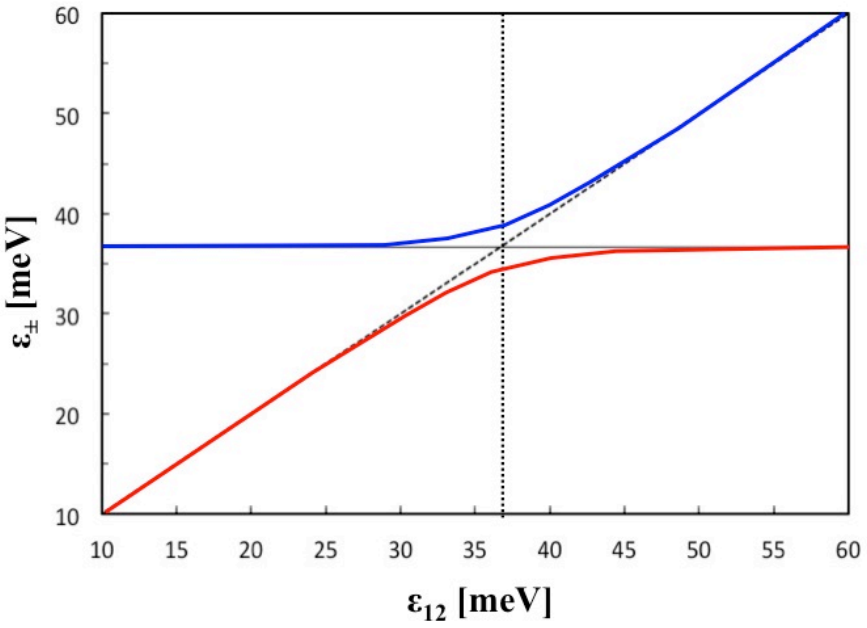

Figure 3.1: Anti-crossing due to electron-LO phonon interaction as a function of ε_{12}. The y-axis indicates the coupled mode energies. The horizontal and the vertical dotted lines are the position of ε_{LO}. The dashed line is the position of non-interacting intersubband transition energy ε_{12}. Energy splitting arises around the LO phonon energy as a result of anti-crossing.

is on the same order as (but larger than) the value, 2W = 4 meV, expected in the above. The argument in the above is based on the simplified two-level model. In order to quantitatively discuss the experimental results here, one needs a theoretical model which is more realistic as will be described in the following section.

3.2 Comparison with Theory

We consider a so called "macroscopic model", or a "dielectric continuum model", by assuming the quantum-well to be a homogeneous dielectric medium [28]. In this model, frequencies in coupled modes, or anti-crossing energy levels, are derived as in the following. First, the resonant process causes the real part of the dielectric constant to change. When the total charge included in the homogeneous medium is kept unchanged, the propagation of electromagnetic wave satisfies,

$$\mathrm{div}[\mathrm{D}(\omega)] = \mathrm{div}[\epsilon(\omega)\mathrm{E}(\omega)] = 0. \tag{3.2}$$

This requires for longitudinal waves to obey the equation

$$\mathrm{Re}[\epsilon(\omega)] = \mathrm{Re}[\epsilon_{\mathrm{LO}} + \epsilon_{\mathrm{ISB}}] = 0, \tag{3.3}$$

where ϵ_{LO} and ϵ_{ISB} are the LO phonon and the intersubband transition contributions to the dielectric function, respectively. The z component (normal to the plane of wells) of the dielectric function is given by

$$\epsilon(\omega) = \epsilon_\infty \frac{\omega^2 - \omega_{LO}^2}{\omega^2 - \omega_{TO}^2 + i\omega 0^+} - \epsilon_\infty \frac{\omega_P^2}{\omega^2 - \omega_{12}^2 + i\omega 0^+}, \tag{3.4}$$

where ω_{12} is the bare frequency of intersubband transition, 0^+ is the damping parameter which is ignored here for simplicity, and ω_P is the plasma frequency of the two-dimensional electron gas, given by

$$\omega_P^2 = \frac{2\omega_{12} d_{12}^2 N_{2DEG}}{\hbar \epsilon_0 \epsilon_\infty L_{QW}}, \tag{3.5}$$

where

$$d_{12} = e \int dz\, \chi_1(z) \chi_2(z) \tag{3.6}$$

is the intersubband dipole. Eq. (3.3) through (3.6) lead to

$$\omega^4 - \omega^2(\omega_{LO}^2 + \omega_{12}^2 + \omega_P^2) + \omega_{LO}^2 \omega_{12}^2 + \omega_P^2 \omega_{LO}^2 \frac{\epsilon_\infty}{\epsilon_s} = 0. \tag{3.7}$$

By using the well known Lyddane-Sachs-Teller relation

$$\omega_{TO}^2 = \omega_{LO}^2 \frac{\epsilon_\infty}{\epsilon_s}, \tag{3.8}$$

Eq. (3.7) can be put into the form

$$\omega^4 - \omega^2(\omega_{LO}^2 + \omega_{12}^2 + \omega_P^2) + \omega_{LO}^2 \omega_{12}^2 + \omega_P^2 \omega_{TO}^2 = 0. \tag{3.9}$$

For convenience of the later discussion, we note that Eq. (3.9) is reduced to

$$\omega^2 = \omega_{12}^2 + \omega_P^2, \tag{3.10}$$

in the limit of $\omega_{LO} \to 0$ (absence of interaction), and to

$$\omega = \omega_{12},\ \ \omega_{LO}, \tag{3.11}$$

in the limit of $\omega_P \to 0$ ($N_{2DEG} \to 0$, absence of electrons). Eq. (3.10) indicates anti-crossing point shifts from ω_{12}^2 to $\omega_{12}^2 + \omega_P^2$ due to "Depolarization shift" [29]. The Depolarization shift originates from the collective nature of intersubband transitions as follows. When electrons absorb external light and are excited via intersubband transition, the profile of their charge density distribution is simultaneously modified. The modification in the charge density profile gives rise to restoring Coulomb force, enhancing the plasma oscillation frequency. As a result, even if interaction with LO phonons did not exist, Depolarization shift of the intersubband transition takes place, following the relation $\omega_0^2 = \omega_{12}^2 + \omega_P^2$. The situation is confirmed on Fig.1.8 which shows that the target wavelength including Depolarization shift is consistent with the photo-response spectrum. At the limit of $\omega_P = 0$, or $N_{2DEG} = 0$, Eq. (3.11) tells us that the intersubband transition and the LO phonons are decoupled, and one should observe the bare (non-interacting) intersubband transition at ω_{12}.

3.2.1 Energy level splitting

We can evaluate the coupled mode frequencies in the upper- and the lower branches by solving Eq. (3.9). In doing this,

$$\hbar\omega_{12} = \frac{3\hbar^2\pi^2}{2m_* L_{QW}^2}, \tag{3.12}$$

and

$$d_{12} = \frac{16 e L_{QW}}{9\pi^2} \tag{3.13}$$

are used for simplicity, which are derived by assuming a symmetric rectangular QW sandwiched by infinite barriers, where L_{QW} is the width of the QW corresponding to the intersubband transition frequency ω_{12}, and N_{2DEG} is the density of the two-dimensional electron gas (2DEG) in the QW with $\epsilon_0 = 8.85 \times 10^{-12}$As/Vm, $\epsilon_\infty = 10.86$. Here $N_{2DEG} = 2.5 \times 10^{11}\text{cm}^{-2}$ is taken as the average value of experimental results.

The theoretical values (Eq.(3.9)) are shown in Fig.3.2 for comparison with experimental values as a function of the bare intersubband transition energy ε_{12}. Equivalent data are re-plotted in Fig.3.3 in terms of dimension-less quantities for convenience of later discussion (Sec.3.2.3 and Fig.3.13). For Fig.3.2, the dashed straight line and the horizontal line indicate, respectively, $\varepsilon_0 = (\varepsilon_{12}^2 + \varepsilon_P^2)^{1/2}$ and the LO phonon energy ε_{LO}. Depolarization shift of the anti-crossing point may be evident.

For comparison with theoretical values, the weighted average of the spectral data were plotted in Fig.3.2. The full theory incorporating the structure of CSIP would involve solving the full problem in the presence of LO phonon and the interference of the wave function. The presently available theories, however, assume a symmetric rectangular QW bounded by infinite barriers, which would give a Lorentzian spectral shape. In addition, individual sharp peaks are sensitive to the change of potential in the graded barrier and the quantum wells. (According to *nextnano3* simulation, the energy of each excited level fluctuates by 0.3–1.0 meV changing the value of each oscillator strength when the potential of the graded barrier varies in a few percentage. The weighted average of the multiple transition energies, $\langle\varepsilon_{12}\rangle$, remains in ± 0.1 meV in the same situation.) Hence the weighted average of the spectral data were compared with the theoretical values.

The experimental value of each spectral band is derived by carrying out the weighted average of the spectral data in Figs. 2.12 through 2.14,

$$\langle\lambda\rangle = \frac{\int \lambda\, I(\lambda)\, d\lambda}{S}, \tag{3.14}$$

where $I(\lambda)$ is the intensity of photo-response, and

$$S = \int I(\lambda)\, d\lambda, \tag{3.15}$$

is the integrated signal intensity for each spectral band. In the calculation, the wavelength range of the upper (ω_+) and the lower (ω_-) spectral bands were divided at the wavelength corresponding to $\omega_0 = (\omega_{12}^2 + \omega_P^2)^{1/2}$, which is given by Eq. (3.10) when absence of interaction. When obtaining the weighted average of the spectral data, we should take into account experimental uncertainty; the systematic uncertainties by the monochromator and by the imperfect calibration of measurements, and the random uncertainty. Figure 3.2 set their total uncertainty as an error bar in the y axis. The result for 15 μm CSIP (Fig.1.8) is also plotted in Fig.3.2, which is only for the upper (ω_+) spectral band because the 15 μm CSIP detected no photo-response in the lower (ω_-) spectral band. For a correspondence of the values in the x axis to the y axis in Fig.3.2, the values of ε_{12} of the data points were taken as the oscillator strength-weighted average of the multiple transition energies from the ground state, $\langle\varepsilon_{12}\rangle$, which their transition energies with relevant oscillator strengths are derived from simulator calculations (*nextnano3*) as seen in Figs.2.4 through 2.6.

The data points representing those experimental values in Fig.3.2 are substantially reproduced by the theoretical values based on the dielectric continuum model. This definitely indicates the validity of the interpretation described in the above. In more detail, however, we notice further that the experimental values of the lower energy branch (ε_-) agree satisfactorily with the corresponding theoretical values, while those of the upper energy branch (ε_+) exhibit a certain deviation towards higher values than the theoretical prediction. The discrepancy will be discussed later in Subsection 3.2.3.

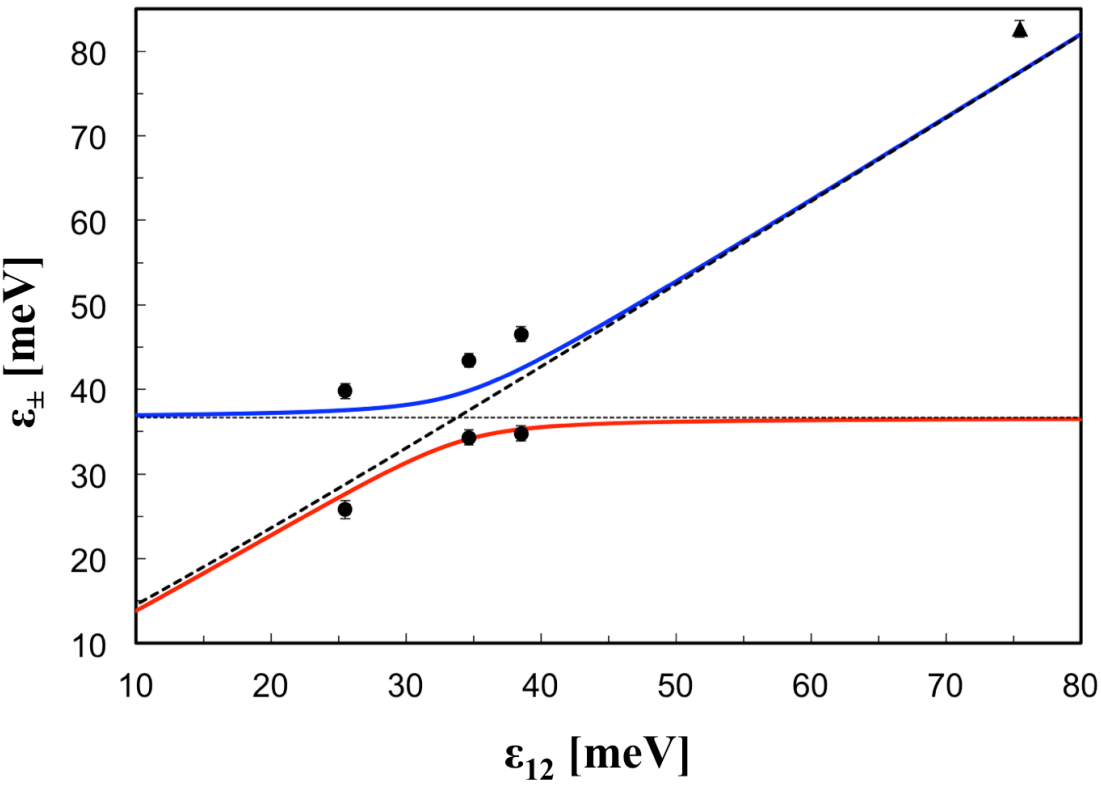

Figure 3.2: Coupled mode energies $\varepsilon_{\pm}$ as a function of the bare intersubband energy ε_{12} in GaAs for $N_{2DEG} = 2.5 \times 10^{11}\text{cm}^{-2}$. The experimental data in the present work (circles) are plotted with the result for 15 μm CSIP (triangle). The top (red) and the bottom (blue) curves are the upper (ω_+) and the lower (ω_-) energy branches obtained from the dielectric continuum model. The dashed line indicates $\varepsilon_0 = \sqrt{\varepsilon_{12}^2 + \varepsilon_P^2}$. The horizontal line shows the LO phonon energy, $\varepsilon = \varepsilon_{LO}$. The anti-crossing point (the intersection of the dashed line with the horizontal line) is shifted from $\varepsilon_{12} = \varepsilon_{LO}$ to $\sqrt{\varepsilon_{12}^2 + \varepsilon_P^2} = \varepsilon_{LO}$ because of Depolarization shift. The values of ε_{12} for the data points were taken as the oscillator strength-weighted average of the multiple transition energies. For all the data points, experimental uncertainty is set as an error bar in the y axis.

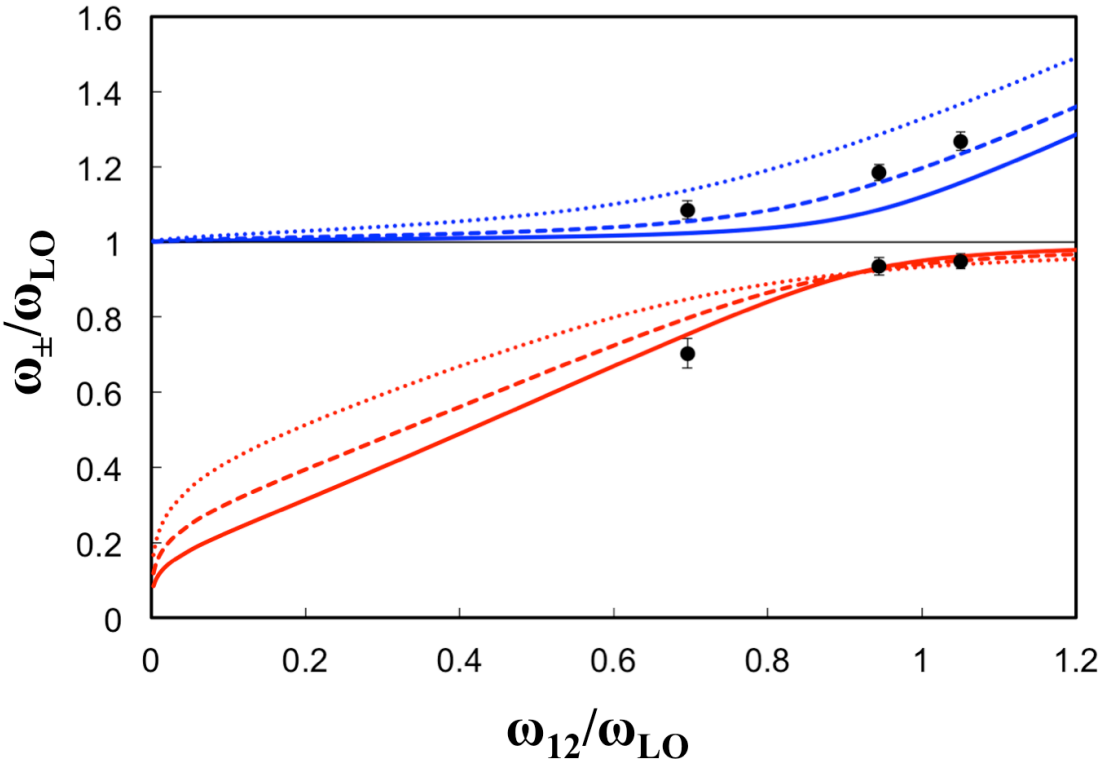

Figure 3.3: The data equivalent to those of Fig.3.2 are shown with values normalized by the LO phonon frequency. The dielectric continuum model is calculated for $N_{2DEG} = 2.5 \times 10^{11}\mathrm{cm}^{-2}$ (solid), $5.0 \times 10^{11}\mathrm{cm}^{-2}$ (dashed), and $1.0 \times 10^{12}\mathrm{cm}^{-2}$ (dotted). The top (red) and the bottom (blue) curves are the upper (ω_+) and the lower (ω_-) frequency branches obtained from the dielectric continuum model. The horizontal line shows the LO phonon frequency, $\omega_\pm/\omega_{LO} = 1$. Theoretical values calculated with different two-dimensional electron density (N_{2DEG}) quantitatively require more than twice for N_{2DEG} than experimentally obtained values. (The experimental values of N_{2DEG} remain in $(2.5 \pm 0.2) \times 10^{11}\mathrm{cm}^{-2}$.)

3.2.2 Dependence on N_{2DEG}

For the rigorous test of the interpretation described in the above, dependence of the spectral response on the electron density, N_{2DEG}, in the upper QW is studied. Equation (3.11) indicates that the coupling strength of the intersubband transition with LO phonons is reduced with decreasing N_{2DEG} and vanishes completely in the limit of $N_{2DEG} \rightarrow 0$. In the experiment, N_{2DEG} can be reduced by applying negative bias voltage, V_{CG}, to metallic photo-couplers (CG1, CG2, CG3 in Fig.2.7 or C1 through C6 in Fig.2.8). Figure 3.4 displays the variation of spectrum with decreasing V_{CG} from 0V down to -250mV for DQW-32, where V_{CG} is applied equally to the six photo-couplers (C1 through C6). Similar data for DQW-36 and DQW-48 are shown, respectively, in Figs.3.5 and 3.6.

It is a common feature of the three samples that the spectrum in the upper frequency branch, ω_+ (shorter wavelengths) shifts its spectral weight towards lower frequencies (the longer wavelength band) with decreasing V_{CG} (or N_{2DEG}) as a result of decrease in the Depolarization shift. On the other hand, the multiple sharp peaks keep the positions with decreasing N_{2DEG} (or ω_P). The influence of N_{2DEG} to the multiple sharp peaks is left unclear. However, the unique behavior of this interference pattern of the intersubband transition will offer a new insight into physics in the QW structure. In the lower frequency branch ω_- (the longer wavelength band), the spectrum does not exhibit substantial shift but its intensity decreases significantly with decreasing V_{CG} (or N_{2DEG}).

As discussed in 3.2.1, the weighted averages of the spectral data were also taken for comparison of the intersubband transition energy with the theoretical model. The weight-averaged wavelength $\langle\lambda\rangle$ of each spectral band (Eq. (3.14)) is derived from the spectra at given values of V_{CG}. The data points in Figs.3.7 through 3.9 show the experimental values of ω_+ and ω_- as a function of N_{2DEG} for DQW-32, DQW-36 and DQW-48, respectively, where ω_+ and ω_- are transformed from the averaged wavelength $\langle\lambda\rangle$ of each band to $\omega_\pm = 2\pi c / \langle\lambda\rangle$ and N_{2DEG} are derived from V_{CG} through the linear relation. The curves in the figures show theoretical values according to Eq. (3.9), where ω_{12} is determined by $\langle\varepsilon_{12}\rangle$, which is the oscillator strength-weighted average of the multiple transition energies from the ground state given by simulator calculations for one electron. Between the maximum and the minimum values of N_{2DEG} in this experiments, the differences of $\langle\varepsilon_{12}\rangle$ remain in 0.3meV. (The curves keep the shape within their line width.)

The experimental data in these figures definitely indicate that the amplitude of energy splitting between the upper and the lower branches is reduced with decreasing N_{2DEG} which is consistent with theoretical prediction. The general trend of experimental ω_+ and ω_- as a function of N_{2DEG} is reproduced substantially by the theoretical curves derived from the dielectric continuum model. Nevertheless, experimental values in the upper branch ω_+ are somewhat higher systematically than the theoretical values. This discrepancy will be discussed later.

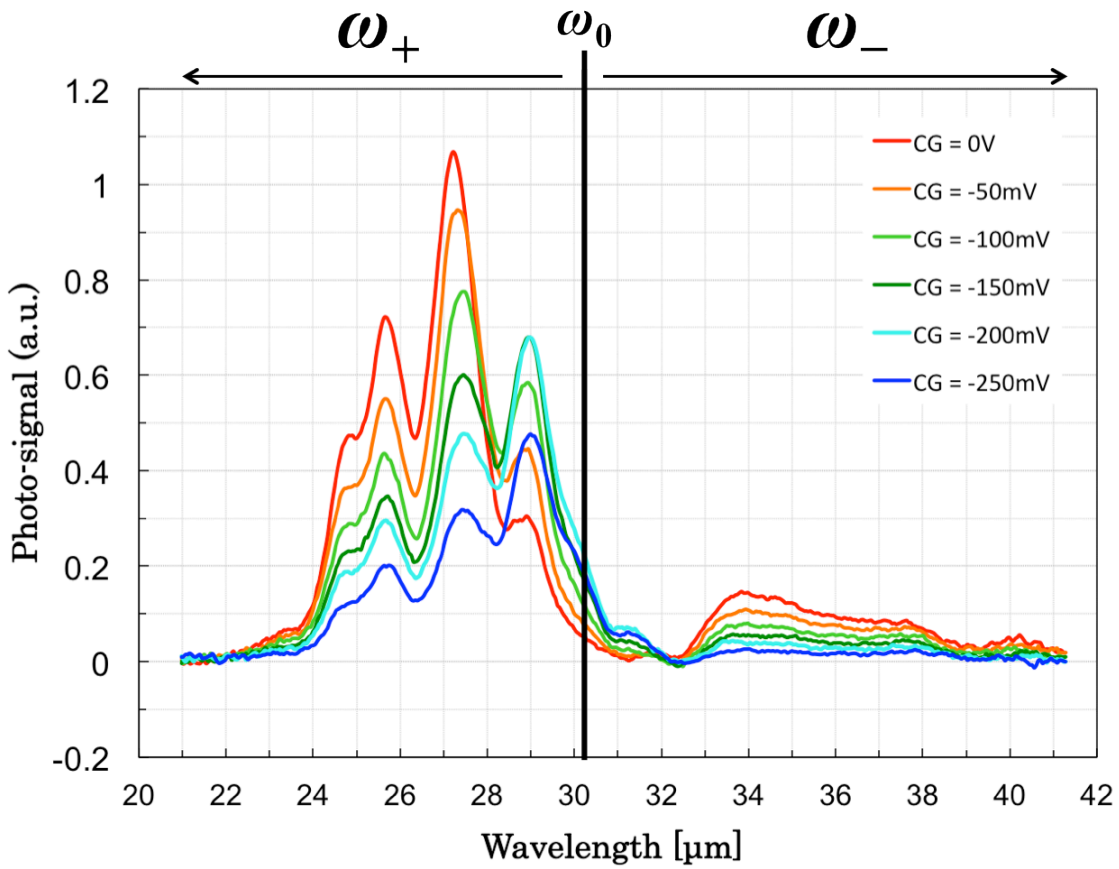

Figure 3.4: Variation of the photo-response spectrum with decreasing V_{CG} for DQW-32. Each color line shows photo-response applied each coupler gate (CG) bias V_{CG} as indicated in the figure. The y-axis (a.u.) preserves relative scale of signal intensities. Photo-responses are split into two spectral bands (ω_+ and ω_-), which are divided at the wavelength corresponding to $\omega_0 = \sqrt{\omega_{12}^2 + \omega_P^2}$.

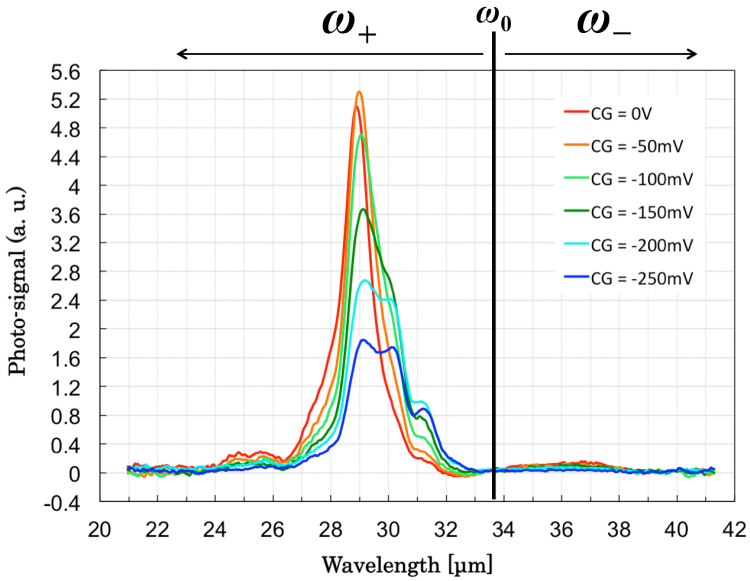

Figure 3.5: Variation of the photo-response spectrum with decreasing V_{CG} for DQW-36. Each color line shows photo-response applied each coupler gate (CG) bias V_{CG} as indicated in the figure. The y-axis (a.u.) preserves relative scale of signal intensities. Photo-responses are split into two spectral bands (ω_+ and ω_-), which are divided at the wavelength corresponding to $\omega_0 = \sqrt{\omega_{12}^2 + \omega_P^2}$.

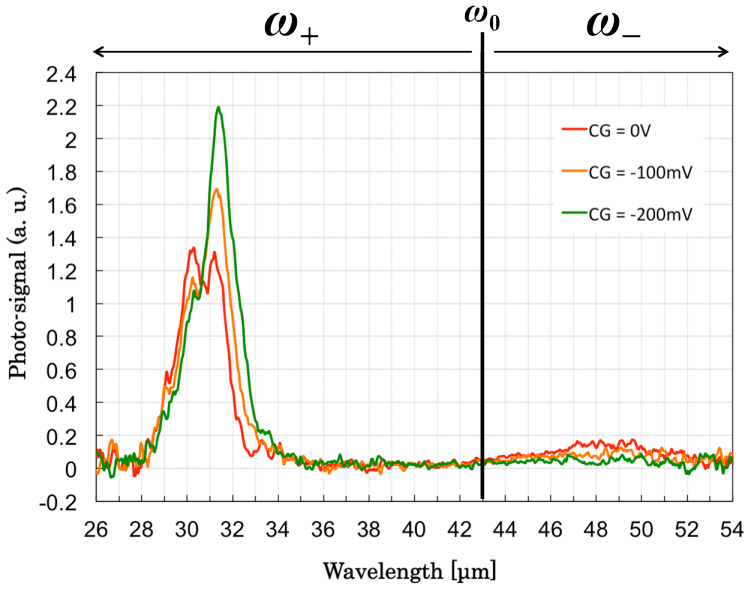

Figure 3.6: Variation of the photo-response spectrum with decreasing V_{CG} for DQW-48. Each color line shows photo-response applied each coupler gate (CG) bias V_{CG} as indicated in the figure. The y-axis (a.u.) preserves relative scale of signal intensities. Photo-responses are split into two spectral bands (ω_+ and ω_-), which are divided at the wavelength corresponding to $\omega_0 = \sqrt{\omega_{12}^2 + \omega_P^2}$.

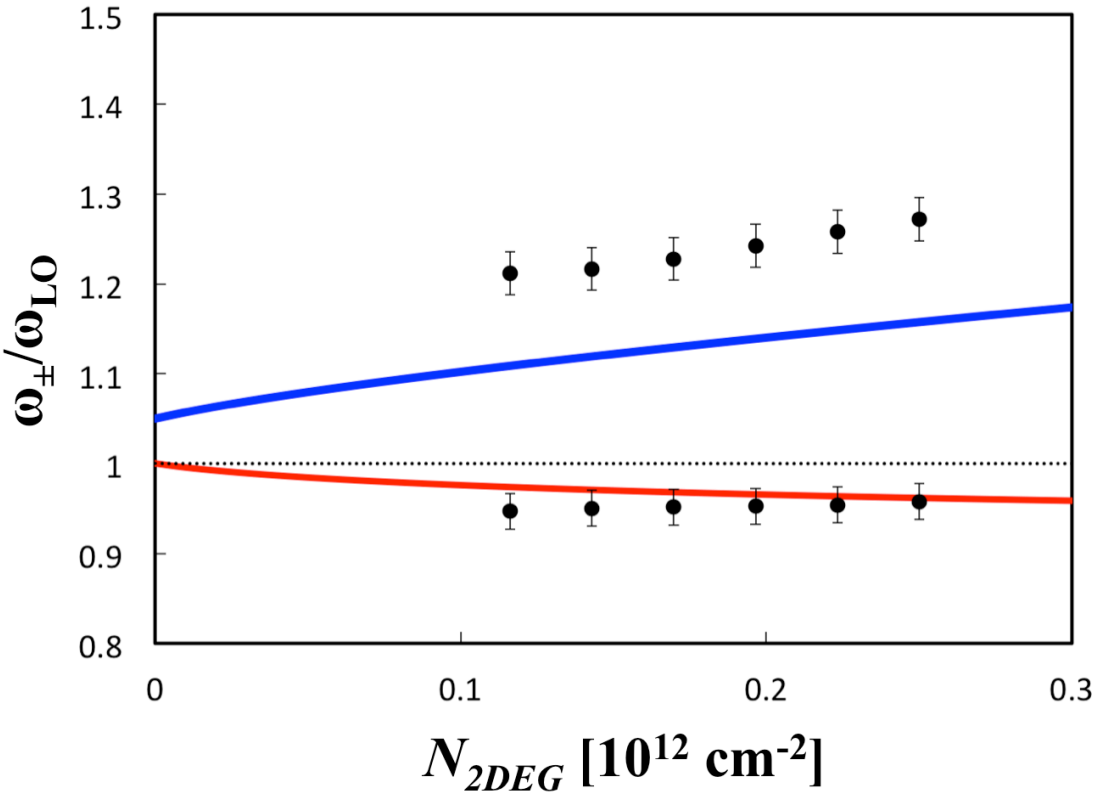

Figure 3.7: Coupled-mode frequencies, ω_+ and ω_-, against N_{2DEG} for DQW-32 (ε_{12} = 38.5 meV). For all the data points, experimental uncertainty is set as an error bar in the y axis. The top (red) and the bottom (blue) curves are the upper (ω_+) and the lower (ω_-) frequency branches derived from Eq.(3.9). The horizontal line shows the LO phonon frequency, $\omega_{\pm}/\omega_{LO} = 1$.

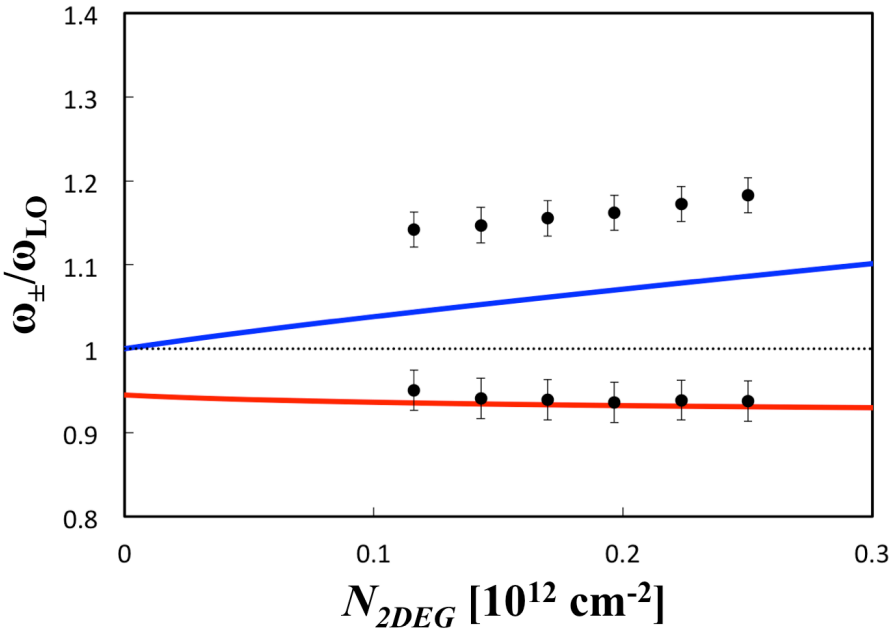

Figure 3.8: Coupled-mode frequencies, ω_+ and ω_-, against N_{2DEG} for DQW-36 (ε_{12} = 34.7 meV). For all the data points, experimental uncertainty is set as an error bar in the y axis. The top (red) and the bottom (blue) curves are the upper (ω_+) and the lower (ω_-) frequency branches derived from Eq.(3.9). The horizontal line shows the LO phonon frequency, $\omega_{\pm}/\omega_{LO} = 1$.

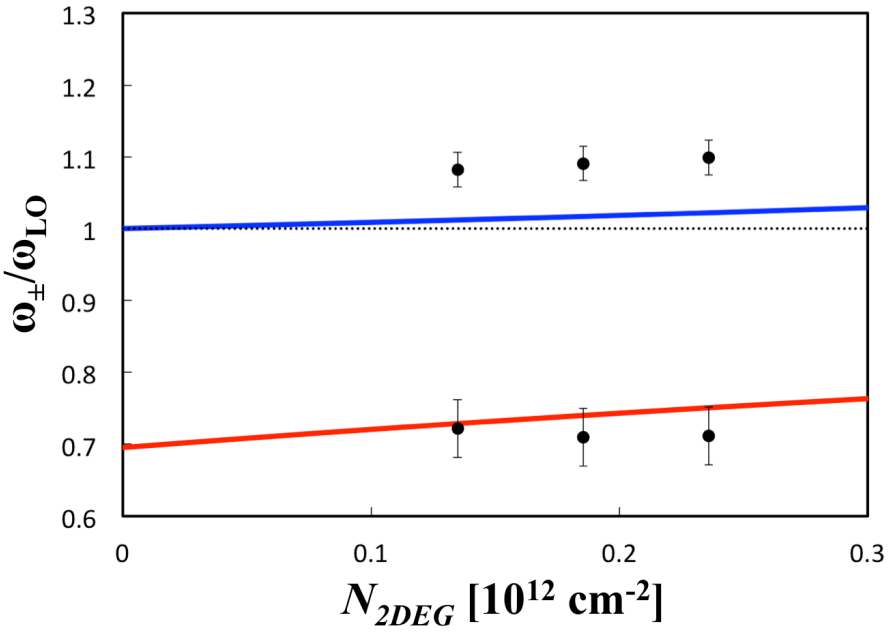

Figure 3.9: Coupled-mode frequencies, ω_+ and ω_-, against N_{2DEG} for DQW-48 (ε_{12} = 25.5 meV). For all the data points, experimental uncertainty is set as an error bar in the y axis. The top (red) and the bottom (blue) curves are the upper (ω_+) and the lower (ω_-) frequency branches derived from Eq.(3.9). The horizontal line shows the LO phonon frequency, $\omega_{\pm}/\omega_{LO} = 1$.

The integrated signal intensity, S (Eq.(3.15)), of each spectral band (ω_+, ω_-) is of particular interest for seeking for a hint of designing THz-CSIPs. The values of S, derived from the data of Figs.3.4 through 3.6, are plotted in Figs.3.10 through 3.12 for DQW-32, DQW-36, and DQW-48 as a function of N_{2DEG}. Solid and dashed lines are guides for eyes. In all of the three samples, linear relationship between S and N_{2DEG} is found in neither of the two spectral bands. Particularly, the intensity of the lower frequency branch (ω_-) in all the samples decreases more rapidly than N_{2DEG}. On the contrary, S of the upper frequency branch (ω_+) for DQW-48 even increases with decreasing N_{2DEG}.

In the present experiments, photo-response in the lower-frequency branch was much weaker in all the crystals DQW-32, DQW-36, DQW-48. This is probably the electrons excited in the lower-frequency branch is prevented to tunnel out of the upper QW because of an unsuitable height of the graded barrier between the upper and the lower QW. Crystal growth with the proper height of the graded barrier can increase photo-signal on the lower-frequency branch. Reducing the tunnel barrier height may weaken the tight confinement of LO phonons in the quantum well, resulting in the decrease in the strong resonant coupling. This control for the tunnel barrier height is expected to enhance the lower-frequency branch that is near the bare intersubband transition frequency ω_{12}. Especially, the influence of LO phonon coupling to the detector sensitivity is left unclear.

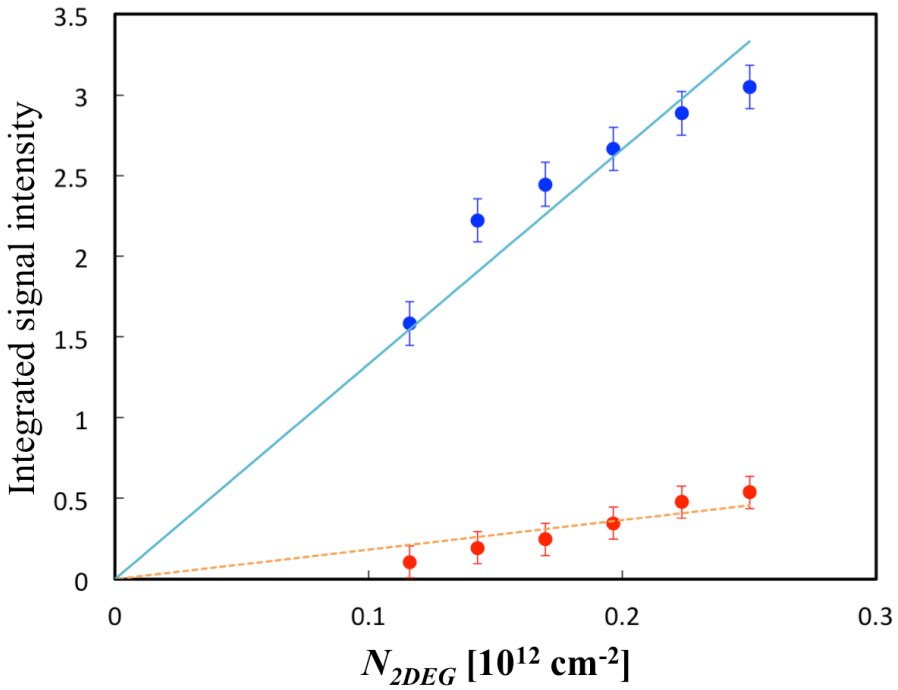

Figure 3.10: Integrated signal intensity S as a function of two-dimensional electron density N_{2DEG} for DQW-32. All experimental data points set integrated intensity obtained from noise signal as an error bar in the y axis. Solid and dashed lines are guides for eyes.

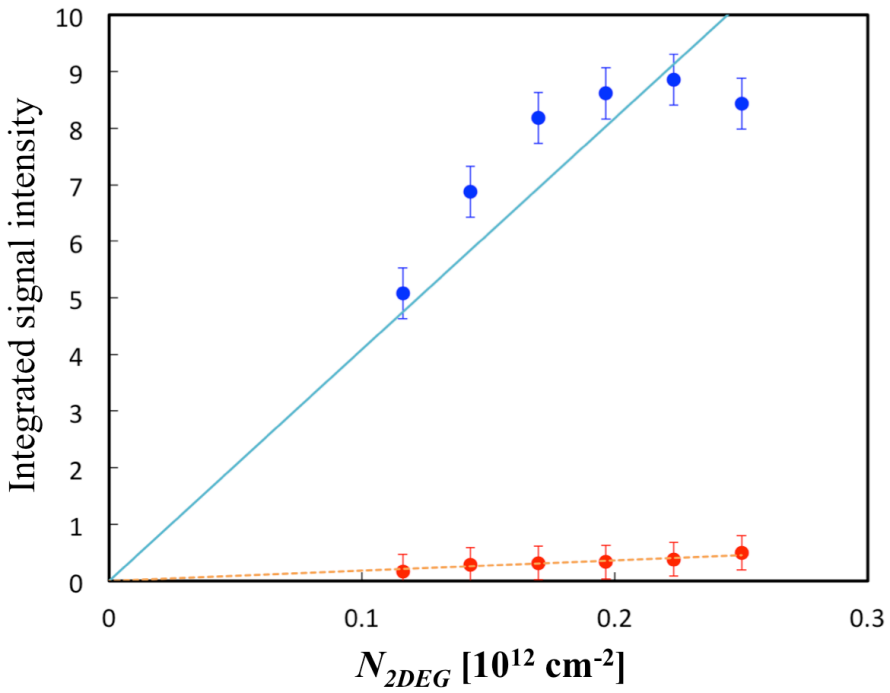

Figure 3.11: Integrated signal intensity S as a function of two-dimensional electron density N_{2DEG} for DQW-36. All experimental data points set integrated intensity obtained from noise signal as an error bar in the y axis. Solid and dashed lines are guides for eyes.

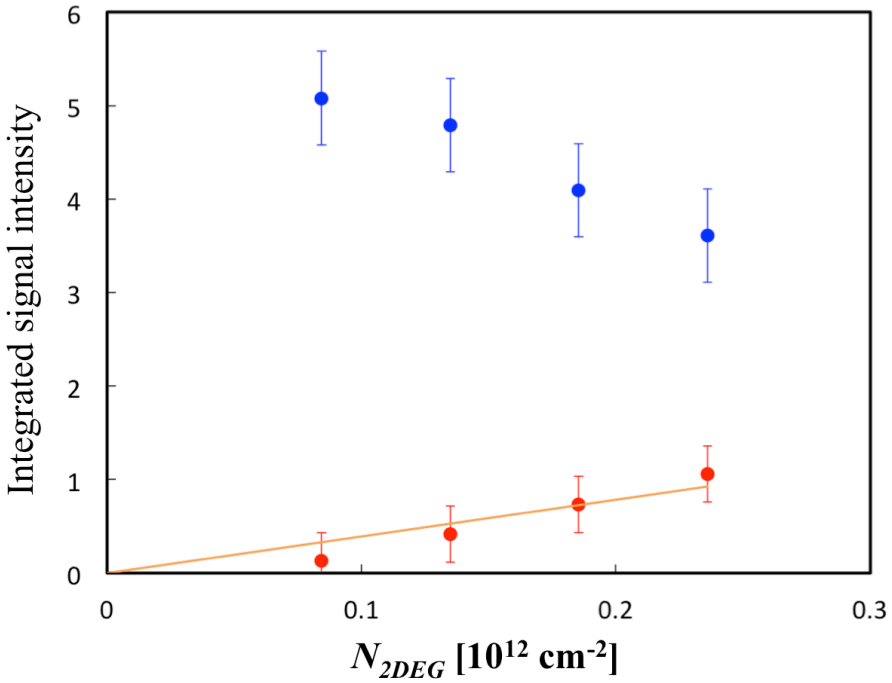

Figure 3.12: Integrated signal intensity S as a function of two-dimensional electron density N_{2DEG} for DQW-48. All experimental data points set integrated intensity obtained from noise signal as an error bar in the y axis. Solid line is the guide for eyes.

3.2.3 Enhancement of LO phonon coupling

Experimentally found level splitting (Figs.3.2 and 3.7 through 3.9) is somewhat larger than the theoretical values predicted by the dielectric continuum model. It is suggested that quantitative agreement between the experimental results and theory might be improved by a "microscopic model", which indicates that the coupling of intersubband transition with LO phonons is remarkably enhanced [30]. The enhancement takes place as a consequence of

- the collective nature of the intersubband transition and
- the natural tight confinement of LO phonons in the QW.

The model describes the intersubband transition under the influence of LO phonons by explicitly treating the full Hamiltonian,

$$\begin{aligned} H &= \sum_q \hbar\omega_{12} b^\dagger_{\mathbf{q}} b_{\mathbf{q}} + \hbar\omega_{LO} r^\dagger_{\mathbf{q}} r_{\mathbf{q}} \\ &+ \sqrt{N_{2DEG}\hbar\omega_{LO}\frac{e^2}{4\epsilon_0\epsilon_\rho}\frac{I(q)}{q}}(b^\dagger_{\mathbf{q}} + b_{-\mathbf{q}})(r^\dagger_{-\mathbf{q}} + r_{\mathbf{q}}) \\ &+ N_{2DEG}\frac{e^2}{4\epsilon_0\epsilon_\infty}\frac{I(q)}{q}(b^\dagger_{\mathbf{q}} + b_{-\mathbf{q}})(b^\dagger_{-\mathbf{q}} + b_{\mathbf{q}}), \end{aligned} \tag{3.16}$$

where the first term represents the electron energy, the second term the LO phonon energy, the third term is the electron-LO phonon interaction [30], and the fourth term is the electron-electron interaction. Here, $b_{\mathbf{q}}$, $b^\dagger_{\mathbf{q}}$ and $r_{\mathbf{q}}$, $r^\dagger_{\mathbf{q}}$ are annihilation and creation operators of electrons and LO phonons, respectively, with in-plane wave vector $\mathbf{q}$, ϵ_ρ is given by

$$\frac{1}{\epsilon_\rho} = \frac{1}{\epsilon_\infty} - \frac{1}{\epsilon_s},$$

with ϵ_s and ϵ_∞ being the static and high-frequency dielectric constant, and $I(q)$ is defined by

$$I(q) = \int dz\, dz'\, \chi_1(z)\chi_2(z)\chi_2(z')\chi_1(z')e^{-q|z-z'|}, \tag{3.17}$$

The third term of Hamiltonian (Eq. (3.16)) shows that the electron-LO phonon interaction is enhanced as N_{2DEG} increases since its amplitude is proportional to $\sqrt{N_{2DEG}}$.

Dashed lines in Fig.3.13 show two eigenfrequencies, ω_+ and ω_-, derived from the diagonalization of the Hamiltonian matrix, as a function of ω_{12} (non-interacting intersubband transition frequency). For comparison, corresponding values derived from the dielectric continuum model (Eq. (3.9)) are shown with solid lines. Experimental values of ω_{12}/ω_{LO} (corresponding to DQW-32, DQW-36, and DQW-48) fall in a range of $\omega_{12}/\omega_{LO} = 0.7 \sim 1.05$ in the figure. Experimental results, however, cannot be directly compared with theoretical values here since the electron density in the experiments ($N_{2DEG} < 2.5\times10^{11}\mathrm{cm}^{-2}$) does not match the value, $N_{2DEG} = 1.0\times10^{12}\mathrm{cm}^{-2}$, assumed in the calculation. Figure 3.13 shows $\omega_\pm$ as a function of N_{2DEG} for $\omega_{12}/\omega_{LO} = 1$.

It is evident in Figs.3.13 and 3.14 that (i) the energy splitting in the experimentally studied range ($\omega_{12}/\omega_{LO} = 0.7 \sim 1.05$) is remarkably larger in the microscopic model, indicating that the intersubband–LO phonon coupling is substantially stronger than that expected in the dielectric continuum model, and (ii) the larger splitting is caused primarily by a large upward shift of the upper frequency branch ω_+, while the lower frequency branches ω_- of the two models give values close to each other. These characteristics are consistent with the features experimentally found in Figs.3.3 and 3.7 through 3.9. As shown in Fig.3.14, experimental data points of DQW-32 indeed fall closer to the theoretical values of microscopic model. The coupling between intersubband

transition and LO phonons is enhanced with increasing N_{2DEG} also in the dielectric continuum model, as noted by the increase of splitting with increasing N_{2DEG} in Figs.3.7, 3.8, and 3.14. However, the enhancement is not sufficiently taken into account in the dielectric continuum model. In the microscopic model, all the relevant phonon modes are taken into account for calculation, but the dielectric continuum model corresponds to a calculation of restricted phonon modes limited to q = 0 and $q_z \rightarrow 0$.

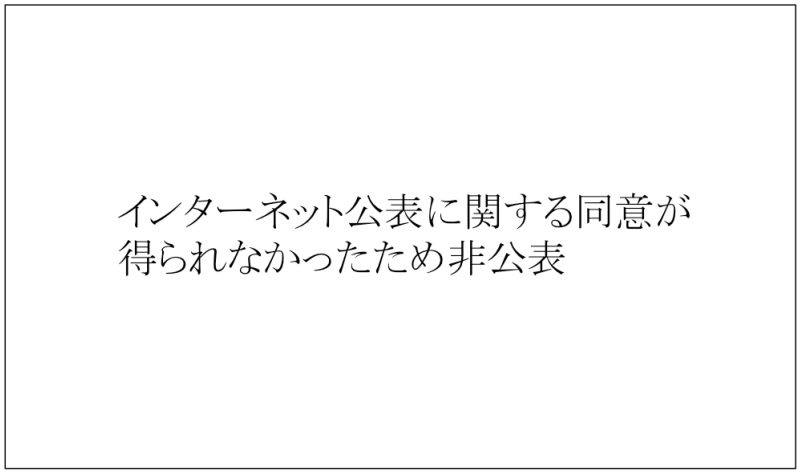

Figure 3.13: Dashed curves indicate eigenfrequencies ($\omega_{\pm}$) derived from the microscopic quantum model [30] (Eq. (3.16)) for $N_{2DEG} = 1 \times 10^{12}\mathrm{cm}^{-2}$ as a function of ω_{12}/ω_{LO} (normalized non-interacting transition frequency). Solid curves are corresponding values derived from the dielectric continuum model (Eq. (3.9)).

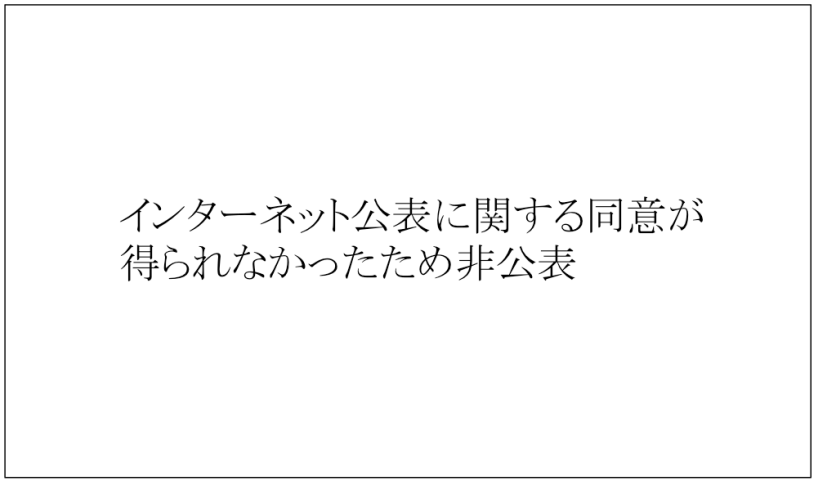

Figure 3.14: Dashed curves indicate eigenfrequencies ($\omega_{\pm}$) derived from the microscopic quantum model [30] (Eq. (3.16)) for $\omega_{12}/\omega_{LO} = 1$ as a function of N_{2DEG}. Solid curves show the corresponding values derived from the dielectric continuum model (Eq. (3.9)). The dots show the data points of DQW-32, where $\omega_{12}/\omega_{LO} = 1.05$ is close to unity.

3.3 Related Experiments

Prior to the present work, two experiments have reported on the LO phonon related anti-crossing behavior. One is on self-assembled InAs quantum dots [31]: Magnetospectrosopic experiment shows energy splitting on the both sides from the bare transition energy due to a resonant interaction between the discrete state and LO phonons (Fig.3.15). This experiment studied the coupling between electrons and LO phonons through the optical method (transmission spectrum) by using quantum dots. On the other hand, the present work with CSIP has measured the anti-crossing behavior in a more direct way (by measuring current response on the site of the interaction of electrons and LO phonons) within the quantum-well structure. Another report is on quantum-wells of quantum cascade lasers (QCL), where transmission spectrum exhibits anti-crossing [28]: The anti-crossing behavior shows up when the difference between the pump and the lasing energies (Raman shift) is comparable to the subband splitting energy as shown in Fig.3.16. This experiment indicate that interaction between electrons and LO phonons gives rise to energy splitting when transition energy is close to the LO phonon energy.

Distinct advantage of CSIP, when compared to other systems in view of a study tool of anti-crossing behavior, is the outstanding sensitivity; viz., photo-response can be clearly seen simultaneously in both of the resonant modes. In Fig.3.16, however, two coupled modes cannot be seen simultaneously, probably because LO phonon-like mode has too weak response to be detected, while the intersubband-like mode is of strong response. In addition, CSIP measures signal current in the lower QW channel applying weak voltage bias (V_{SD} = 10mV). Thanks to this mechanism, CSIP can read out photo-response preserving the coupled mode states in the double QW. Aside from the aspect of fundamental material research, significant message of the present work may be the importance of the strong coupling with LO phonons in designing highly sensitive THz-CSIPs. This is because unavoidable strong coupling between intersubband transition and LO phonons causes remarkable modification in both the detection wavelength and probably the detection sensitivity.

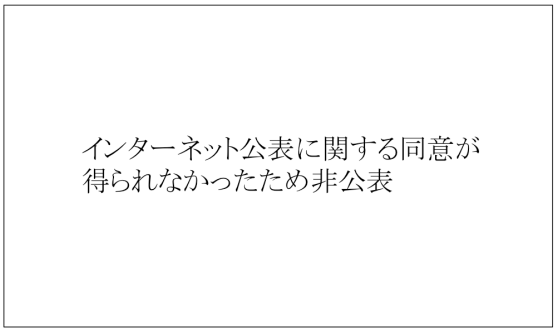

Figure 3.15: Magnetic field dispersions of the resonance (full circles) [31]. The dashed lines are the calculated dispersions from the simple perturbation approach. The solid lines show the calculated coupling of electron-LO phonon interaction. Energy splitting is found to increase with B because of the Zeeman effect. The interaction of the different transitions with LO phonons provokes two anti-crossing. The insets shows the calculated time dependence of the survival probability of the two non-interacting (zero-phonon) states (Rabi oscillation).

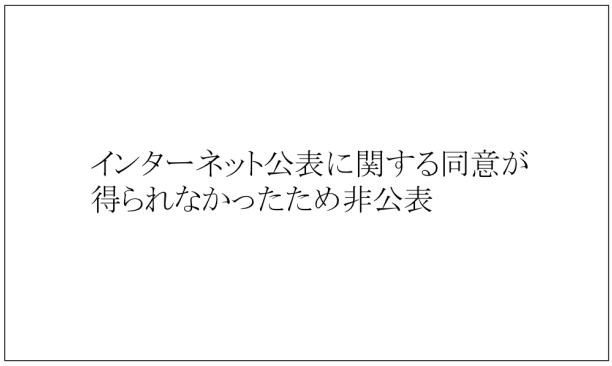

Figure 3.16: (a) Emission peak position vs. pump position for the QCLs [28]. Each type of symbol represents one sample. The inset to the figure shows the transmission spectrum for one sample. (b) Difference between pump and emission photon energies, i.e. Stokes Raman shift, vs. intersubband energy (1-to-2) [28]. The values of the y-axis are obtained from results shown in (a). The curves (solid for GaAs phonon and dashed for AlAs-like phonon mode) are calculated from the model. The two horizontal lines indicate the positions of the LO phonons, while the two vertical dotted lines show the expected anti-crossing positions.

3.4 Brief Summary of This Chapter

By using CSIP for the target wavelength of 32, 36, 48 μm, we observed photo-response spectra in the different wavelength regions from the target wavelength. In this chapter, we discussed the origin of photo-response that consists of two distinctly separated spectral bands.

In GaAs crystal, strong coupling process of electrons with LO phonons leads to the formation of hybridized "polaron" state, that is a superposition of the two states; the state with an electron in the excited subband and zero LO phonon $|\, \mathrm{e}, 0_{LO}\rangle$, and the state with the electron in the ground subband and one LO phonon $|\, \mathrm{g}, 1_{LO}\rangle$. The polaron states can give rise to level anti-crossing as the intersubband energy difference ε_{12} is close to the LO phonon energy ε_{LO}.

The scenario of anti-crossing is justified only when the electron/phonon system is in a quantum-mechanically undisturbed state to assure coherent interaction between electrons and LO phonons. This condition is violated in widely applied QWIPs, but is satisfied in the present system of CSIP. This is because excited electrons are preserved coherently in isolated region consisting of the upper and the lower quantum wells with a lifetime experimentally evaluated to be about 4 psec, which is long enough for the formation of coupled polaron state. It is hence probable that the intersubband transition in CSIP coherently couples with LO phonons.

In order to quantitatively discuss the experimental results here, we considered a theoretical model. The experimental values are substantially reproduced by the theoretical values based on the dielectric continuum model. This definitely indicates the validity of the interpretation described as the formation of coupled polaron state.

The coupling strength of polaron states should be weakened if the density of electrons relevant to the intersubband transition decreases. For more detailed test of the interpretation of the formation of coupled polaron state, dependence of the anti-crossing on the two-dimensional electron density (N_{2DEG}) in the upper QW is studied. The experimental data indicate that the amplitude of energy splitting between the upper and the lower branches is reduced with decreasing N_{2DEG} which is consistent with theoretical prediction. The experimentally obtained coupled-mode frequencies (ω_+ and ω_-) as a function of N_{2DEG} is reproduced substantially by the theoretical curves derived from the dielectric continuum model. In more detail, however, we notice further that the experimental values of the lower energy branch (ω_-) are in good agreement with the corresponding theoretical values, while those of the upper energy branch (ω_+) exhibit a certain deviation towards higher values than the theoretical prediction.

It is suggested that quantitative agreement between the experimental results and theory might be improved by the microscopic model, which indicates that the coupling of intersubband transition with LO phonons is remarkably enhanced. As a result, this microscopic quantum model gives rise to larger level anti-crossing than that of the dielectric continuum model. Experimental data points indeed fall closer to the theoretical values of microscopic model. The microscopic model could explain the difference between the experimental results and the prediction of the dielectric continuum model.

Chapter 4

Conclusion

We have discussed the strong resonant coupling due to interaction between electrons and LO phonons. Spectral measurement by using charge sensitive infrared phototransistors (CSIP) found evidence of anti-crossing due to interaction of intersubband transition with LO phonons.

Our aim is to develop CSIP for astronomical applications for the wavelengths of 30 – 60 μm. Teraherz (THz) or Far-infrared (FIR) region ($\lambda \sim 30$ – 300 μm) offers the opportunity to probe the process of star-, planet-, and galaxy-formation. In addition, the wavelength range of 30 – 60 μm is important for the study of protoplanetary disks, which provide the clue to understand the planetary-formation process. However, spectroscopic observations in the wavelength range of 30 – 60 μm, have been very much limited for the lack of sensitive detectors in this range.

Hence, in this thesis, we focused on the application of CSIP for the wavelength range of 30 – 60 μm, which has rich astronomical information yet unexplored. CSIP is a quantum-effect device implemented in a GaAs/AlGaAs double QW structure. The operation mode of CSIP is as follow: The upper quantum-well (QW) in the double QW structure is positively charged up by photo-excitation via intersubband transition. This conduces to increase in the conductance of the lower QW channel. In other words, the electrically isolated upper QW serves as a photo-sensitive gate to the source-drain channel formed by the lower QW. This mechanism gives extraordinary high photoconductive gain. Hence CSIP is the promising detector with high sensitivity in the FIR. CSIP has been well established in the mid-infrared region (12 - 20 μm), achieving Noise Equivalent Power (NEP) of 7×10^{-20} W/$\sqrt{\text{Hz}}$, which is much better than those of conventional semiconductor detectors.

Widening the width of the upper QW can shift the target wavelength to longer region. However, within the wavelength region of 30 – 60 μm, there is a wavelength range, called "Reststrahlen band", in which the light is strongly reflected and absorbed due to strong coupling of photons with phonons. The wavelength range of the Reststrahlen band is bounded by the Longitudinal Optical (LO) phonon frequency, ω_{LO}, and the Transverse Optical (TO) phonon frequency, ω_{TO}. In GaAs, the Reststrahlen band is located in the range between 33.8 μm (LO) and 36.8 μm (TO) at 4K. Since the light does not penetrate substantially into the material, photo-response is completely absent in the Reststrahlen band, as exemplified for widely used Quantum-Well Infrared Photodetctors (QWIP). In the case of CSIP, however, the photo-active upper QW is located immediately below the GaAs surface (about 100 nm depth). The photo-active region is well within the penetration depth (around a few microns) of radiation in the Reststrahlen band. Hence CSIPs are expected to exhibit finite response to the radiation in the Reststrahlen band: The response is of particular interest because of strong interaction of electrons and LO phonons (Polaron effect) and strong interaction between photons and TO-phonons (Polariton effect). It is important to experimentally clarify how these interactions play their roles in the photo-response mechanism.

For this sake, we have designed and fabricated CSIPs especially for the Reststrahlen band in this work. The upper QW width along with the overall crystal structure was so designed that

the target wavelength falls in the Reststrahlen band. The target wavelengths of the crystals were designed to be 32, 36 and 48 μm. As a result, we observed photo-response in all of the three devices. Moreover, spectral measurement revealed that photo-response consists of two distinctly separated spectral bands. One of the bands substantially overlaps with the Reststrahlen band, while the other was found in shorter wavelength region than the target wavelength.

In GaAs crystal, conduction electrons strongly couple to longitudinal optical (LO) phonons due to Coulomb interaction. Due to the interaction, an electron in a QW repeats coherent process of virtual emission and absorption of LO phonons, leading to the formation of hybridized "polaron" state, that is a superposition of the two states; the state with an electron in the excited subband and zero LO phonon $|\,\mathrm{e}, 0_{LO}\rangle$, and the state with the electron in the ground subband and one LO phonon $|\,\mathrm{g}, 1_{LO}\rangle$. The polaron states give rise to level anti-crossing as the intersubband energy difference ε_{12} is close to the LO phonon energy ε_{LO}.

The scenario of anti-crossing is justified only when the electron/phonon system is in a quantum-mechanically undisturbed state to assure coherent interaction between electrons and LO phonons. This condition is violated in widely applied QWIP, but is satisfied in the present system of CSIP. This is because excited electrons are preserved coherently in isolated region consisting of the upper and the lower quantum wells with a lifetime experimentally evaluated to be about 4 psec, which is long enough for the formation of coupled polaron state. It is hence probable that the subband transition in CSIP coherently couples with LO phonons.

In order to quantitatively discuss the experimental results here, we considered the theoretical model. The "dielectric continuum model" describes dielectric constant due to interaction between intersubband transition and LO phonons in a homogeneous medium. The experimental values are substantially reproduced by the theoretical values based on the dielectric continuum model. This definitely indicates the validity of the interpretation described in the above.

The coupling strength of polaron states should be weakened if the density of electrons relevant to the intersubband transition decreases. For rigorous test of the interpretation described in the above, dependence of the anti-crossing on the two-dimensional electron density (N_{2DEG}) in the upper QW was studied. The experimental data definitely indicate that the amplitude of energy splitting between the upper and the lower branches is reduced with decreasing N_{2DEG} which is consistent with theoretical prediction. The general trend of experimentally obtained coupled-mode frequencies (ω_+ and ω_-) as a function of N_{2DEG} is reproduced substantially by the theoretical curves derived from the dielectric continuum model. In more detail, however, we notice further that the experimental values of the lower energy branch (ω_-) agree satisfactorily with the corresponding theoretical values, while those of the upper energy branch (ω_-) exhibit a certain deviation towards higher values than the theoretical prediction.

It is suggested that quantitative agreement between the experimental results and theory might be improved by the microscopic model, which indicates that the strong coupling of intersubband transition with LO phonons is remarkably enhanced. As a result, this microscopic quantum model gives rise to larger level anti-crossing than that of the dielectric continuum model. Experimental data points indeed fall closer to the theoretical values of the microscopic model. The microscopic model could explain the difference between the experimental results and the prediction of the dielectric continuum model.

In order to develop THz-CSIP for the wavelengths of 30 – 60 μm, we have to pay careful attention to the strong coupling between intersubband transition and LO phonons. It is crucial for THz-CSIP to enhance photo-signal in the ω_- branch suppressing photo-signal in the ω_+ branch. The one approach to realize this condition is the reduction of the height of the graded and the tunnel potential barrier of CSIP.

This paper have reported detailed experimental evidence that intersubband transition and LO phonons are resonant in the strong coupling regime by using the novel detector, CSIP. Anti-crossing has been clearly seen in our spectral measurement in the vicinity of the Reststrahlen

band. The experimental values for frequency splitting are substantially reproduced by the theoretical values based on the dielectric continuum model. The LO phonon-like mode (the mode with frequency nearer ω_{LO}) is expected to have smaller photo-response compared to that of the intersubband transition-like mode, since the energy of LO phonon-like mode is spent for lattice scattering rather than intersubband transition. Previous experiments on Quantum-well detectors showed small anti-crossing, showing photo-response only for the intersubband transition-like mode. The current result is the first experimental results to show the two polaron states in the strong coupling regime. This is partly because the lifetime of the resonant coupled modes is long enough to observe photo-response because CSIP can read photo-current keeping coupled quantum states in the double QW. Thanks to high sensitivity and the unique structure of CSIP, we observed the strong coupling in the both $\omega_{\pm}$ modes.

Appendix
Optimization of Wafer Characteristics for THz-CSIP

CSIPs have been developed at the wavelength of 12 to 45 μm [32]. Shorter-wavelength CSIPs (12 – 19 μm) have been successfully applied for the development of novel passive near-field optical microscopy with unprecedented resolution [33]. Unfortunately, longer-wavelength CSIPs (30 – 45 μm; THz-CSIPs), which have been developed for our interested wavelength region, had suffered from substantially lower sensitivity than those for 15μm [34]. We investigated the cause of this lower sensitivity prior to the study described in this paper. In this appendix section, we describe the improvement of the sensitivity of THz-CSIPs by optimizing wafer structures. Most of the description in this appendix have been published as [35]. The published paper is available at Springer via http://dx.doi.org/10.1007/s10909-014-1140-6.

A.1 Sample Wafers

We tested 9 types of GaAs/AlGaAs double QW heterostructure crystals, whose characteristics are summarized in Table A.1 (sample A – I hereafter). All the samples were grown via molecular-beam epitaxy (MBE). The upper QW thickness was designed as 20 nm for some crystals whose targeted wavelength was 45 μm, and as 23 or 24 nm for other ones with the target wavelength of 52 μm. Following the aforementioned discussion, the Si-doping level for the upper QW was designed so that the electron density of the upper QW to be $n_U = (1.4 - 3.5) \times 10^{11}\mathrm{cm}^{-2}$, which corresponded to $\varepsilon_F - \varepsilon_1 = 4.7 - 12$ meV. Both designed and measured electron densities n_U are indicated in Table A.1. We normally designed the potential barrier between the upper and the lower QW as a graded $Al_xGa_{1-x}As$ layer: Aluminum composition x linearly decreases in the direction from the upper QW to the lower QW. All the lower QW consist of GaAs except for the samples A and B. The samples A and B were designed to have more simple growth pattern to achieve proper carrier redistribution, and whose potential barriers and lower QWs were designed as a layer with constant material composition of $Al_xGa_{1-x}As$, where x was constant values of 0.04 (Sample A) and 0.02 (Sample B). To achieve high values of μ_L with relatively low values of n_L, the lower QW was remotely doped with Si for all the samples with a spacer layer, whose thickness was $\sim$ 30 nm.

The devices were fabricated by using a standard photolithography technique. The 2DEG layers were defined by wet mesa etching, and ohmic contacts were formed by alloying with 200 nm AuGeNi layer. The photo-active region in the upper QW, whose length and width were L $\times$ W = 150 μm $\times$ 10 μm, was defined by the negative biasing of the isolation gates (IGs) (Fig.A.1). Electrons in the upper QW can be excited only by the electric field perpendicular to the two-dimensional layer (hereafter we refer this direction as the z-direction) because the dipole moment in the z-direction contributes to the excitation. To generate the electrical field component in the z-direction, several dipole antennas were deployed on top of the photo-active region (Fig.A.1).

Table A.1: Crystal structure parameters for THz-CSIP.

Sample name	Upper QW (GaAs)				Lower QW ($Al_xGa_{1-x}As$)		
	Well width [nm]	Si-well doping *1 [10^{17}/cm^3]	n_U *2 [10^{11}/cm^2]	μ_U [10^4cm^2/V s]	x	n_L [10^{11}/cm^2]	μ_L [10^4cm^2/V s]
A	20	2.5	2.6 (3.5)	0.25	0.04	not detected	not detected
B	20	2.5	3.6 (3.5)	0.39	0.02	1.5	1.1
C	20	1.5	2.0 (2.1)	0.91	0 (GaAs)	4.1	13
D	20	1.0	not detected (1.4)	not detected	0 (GaAs)	3.2	4.6
E	20	1.5	2.2 (2.1)	0.43	0 (GaAs)	3.9	16
F	20	1.5×10^{12}/cm^2	0.6 (1.8)	19	0 (GaAs)	2.2	41
G	20	2.0×10^{12}/cm^2	1.4(2.4)	8.3	0 (GaAs)	2.0	37
H	23	-	1.9 (1.7)	3.9	0 (GaAs)	2.1	3.7
I	24	-	not detected (1.7)	not detected	0 (GaAs)	1.2	2.7

*1 Remote delta doping for Sample F and G, and no well-in doping for Sample H and I.

*2 The designed n_U are indicated in the parentheses for respective crystals.

The lengths of the dipole antennas were different from each other, so that the antennas were sensitive for different wavelengths of the incident radiation. The dipole antennas were separated by obliquely-deposited 20nm/80nm NiCr/Au layers (Fig.A.1(b)). The efficiency of these antennas may not be as high as that of the photo-couplers used above (Fig.2.8). However, we used this antennas for this measurement to compare among different samples at first, since the fabrication procedure was much simpler than the photo-couplers, as the antennas were fabricated only by photolithography.

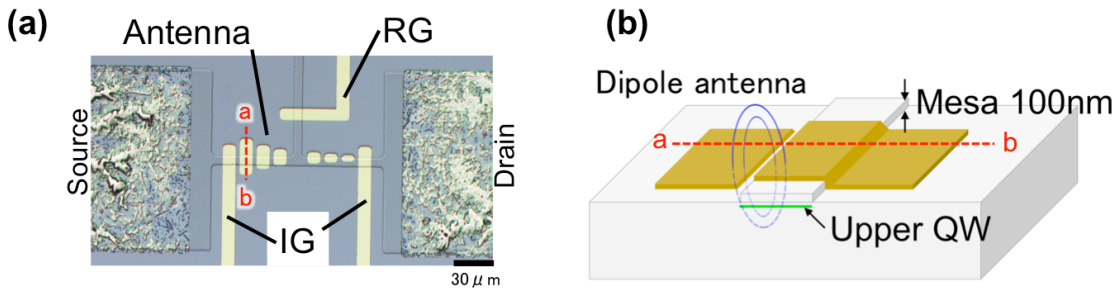

Figure A.1: (a) A micrograph of the device. (b) Schematic representation of one of the antennas.

A.2 Experimental Results and Discussion

Here we describe the experimental results of the THz-CSIP, and how to derive the electron density and the mobility and to estimate the sensitivity.

All the measurements were carried out at 4.2 K with V_{SD} = 10 mV. The device was placed at the end of a 1 m-long metal light pipe, which was inserted in a liquid Helium tank. The intensity of the incident radiation was continuously changed by pulling up or pushing down a black polyethylene plug into the light pipe, so that the temperature of the plug was continuously changed from 300 K to 4.2 K and the plug served as a black-body radiation source with those temperatures.

The measurement results are summarized in Table A.1. Photo signal detection was achieved with Samples B and E. Figure A.2(a) shows the source-drain current of sample E as a function of

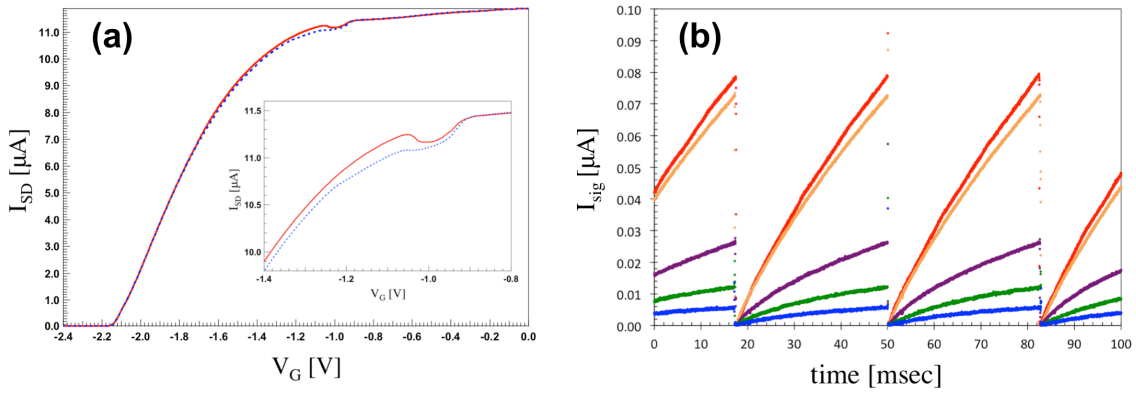

Figure A.2: (a) Source-drain current against the gate bias voltage (V_G) in Sample E: The solid line and the dotted line correspond, respectively, to the conditions with and without the radiation. The inset shows magnified view. (b) Time traces of photo-signals at $V_G = -1.0$ V. Different curves correspond to different intensities of radiation, where the strongest one corresponds to 300 K radiation incident from the top of the light pipe and weakest one to the dark (4.2 K radiation). All the data are obtained from Sample E.

the gate bias voltage, which was applied to both IGs and RG in the conditions with and without the 300 K radiation. A small dip of the curve around $V_G = -1.0$ V indicates the threshold voltage (V_{th}). Below V_{th}, the photo-active region of the upper QW is electrically isolated (serving as a floating gate). The inset in Fig.A.2 (a) shows a bump of the current under the 300K radiation below the threshold voltage ($V_G < -1.0$ V), which is the photo signal by the accumulation of positive charge in the photo-active region. Figure A.2 (b) shows the time traces of the photo-current for sample E under the reset operation, where a brief positive pulse (amplitude: 1.0 V, duration: 2μs, frequency: 30 Hz) was applied to the RG.

The number of photo-induced charges n_p on the isolated upper QW island can be evaluated from the maximum amplitude of the saw-tooth signal current I_{sig} (Fig. A.2(b)) by the relation:

$$I_{sig} = n_p \Delta I_e, \tag{A.1}$$

where ΔI_e is given by Eq.(1.6). The rate of photo-induced charges accumulation N_p is thereby derived to be $N_p = 2.6 \times 10^6$ s^{-1}. The number of incident photon is estimated by the following equation:

$$\Phi = \left[\frac{B(\lambda, T)\Omega\Delta\lambda}{hc/\lambda}\right] S\,[\mathrm{sec}^{-1}], \tag{A.2}$$

where h is the Planck's constant, Ω is the solid angle viewed from the detector to the light source, $\Delta\lambda$ is the bandwidth of the detector, S is the photo-active area, and $B(\lambda, T)$ is the Plank 's law, which is described as the following:

$$B(\lambda, T) = \frac{2hc^2}{\lambda^5}\left[\exp\left(\frac{hc}{\lambda k_B T}\right) - 1\right]^{-1} [\mathrm{Js}^{-1}\mathrm{m}^{-2}\mathrm{sr}^{-1}\mathrm{m}^{-1}]. \tag{A.3}$$

Φ can be evaluated from Eqs.(A.2) and (A.3), by substituting experimental values of $\lambda = 45\mu$m, T = 300K, $\Omega = S/d^2$ (S: inner area of the light pipe, d: distance from the detector to the end of the pipe). Taking into account the throughput of the light pipe of 10%, the quantum efficiency is derived by

$$\eta = \frac{10 \times N_p}{\Phi}. \tag{A.4}$$

NEP of a given detector is derived from the following equation ([1]):

$$NEP = \frac{P}{S/N\sqrt{\Delta f}} = \sqrt{\langle I_n^2\rangle \Delta f}\left(\frac{h\nu}{eG}\right), \tag{A.5}$$

where P is the incident radiation power on the photo-active area, S/N is the signal-to-noise ratio, Δf is the measurement bandwidth, and $\langle I_n^2\rangle$ is the noise current in bandwidth of Δf. We estimate NEP $\sim 10^{-15}$ W/ $\sqrt{\text{Hz}}$ for the measurement shown in Fig.A.2, whose P$\sim$100 pW, S/N $\sim 10^2$, and Δf $\sim$100kHz. A sensitivity improvement of more than one order of magnitude has been achieved from the earlier measurements [34]. This NEP can be improved as low as $\sim 10^{-18}$ W/ $\sqrt{\text{Hz}}$ if we decrease the detector size to that of the 15 μm CSIP devise ($L \times W = 16 \times 4\ \mu\text{m}^2$), expected from NEP $\propto W^{1/2} \times L^{3/2}$ relation derived from Eq.(A.5). However, this expected NEP is still ten times worse than that of the 15μm CSIP.

We obtained electron density and mobility from data of the source-drain current vs. gate bias voltage shown Fig.A.2(a). When $V_G > V_{th}$ (above the threshold voltage), the isolated upper QW island forms a capacitor with an ohmic contact on the surface. As V_G decrease below V_{th}, the lower QW starts to form a capacitor with the ohmic contact. Analogous to $Q = CV$, electron density is given by

$$eN = \frac{\varepsilon\, S\, V_{th}}{d_1}, \tag{A.6}$$

where N is the number of $S = L \times W$, $\varepsilon = \varepsilon_r\varepsilon_0$ (ε_r: relative permittivity, ε_0: permittivity of vacuum), and d_1 is the distance between the surface and the upper QW. By substituting $n_U = N/S$, Eq.(A.6) is rewritten as

$$n_U = \frac{\varepsilon V_{th}}{e d_1}, \tag{A.7}$$

Moreover, analogous to $j = en\mu E$, mobility is given by

$$\frac{I_U}{W} = e\, n_U\, \mu_U\, \frac{V_{SD}}{L_{SD}}, \tag{A.8}$$

where I_U is the current difference measured between V=0 and V=V_{th}. The mobility in the upper QW (μ_U) can be derived from Eq.(A.8) with n_U obtained from Eq.(A.7). We define a voltage that source-to-drain current falls to zero, as V_{th2}. For the lower QW, n_L is derived from Eq.(A.7) replacing V_{th} and d_1 with V_{th2} and d_2, where d_2 is the distance between the surface and the lower QW. The mobility in the lower QW (μ_L) is also derived from Eq.(A.8) replacing I_U and n_U with I_L and n_L, respectively, where I_L is the current difference measured between V_{th} and V_{th2}. Table.A.1 lists experimental values of the electron density and the mobility for the upper and the lower QW.

The results of this measurement for nine samples can be summarized as follows:

- Photo signal has been detected with Samples B and E.
- Experimental values of n_U in several samples are smaller than the designed values. This is probably because of the imperfection of the crystal fabrication and the resultant localization effect of electrons.
- Sample A does not show photo-signal because the conduction through the lower QW is not detectable. This is because the electrons in the $Al_xGa_{1-x}As$ layer (x = 0.04) are nearly localized due to alloy scattering.
- The photo-signal in sample B is smaller than that in sample E as the result of the lower value of μ_L.
- In Sample D and I, the upper QWs show deficit in the electron numbers because the Si doping concentration is not sufficient for these samples.
- In Sample F and G (remote delta doped), n_U is found to be low and non-uniform, resulting in no photo-signal. Crystal imperfections in the barrier layers give rise to electron traps reducing n_U.

- In Sample H, μ_L is spatially non-uniform and much less than expected, and thus photo-signal cannot be detected.
- Sample C is a unique example, in which both the upper and the lower QWs are reasonably formed but the photo-signal is absent.

To investigate this puzzle of Sample C, we have carried out additional measurements. For sample C, we confirmed that the recombination lifetime τ_{life} was exceptionally short.; $\tau_{\text{life}} \approx 150\mu$s. In other words, the upper QW was not electrically isolated due to very small but finite electrical leakage to the lower QW or to the ohmic contacts. The leakage mechanism is unclear at present and left for future investigation.

A.3 Summary of This Work

We have improved performance of THz-CSIPs (45 μm) by optimizing the design of GaAs/AlGaAs double QW structures. Particularly, we found that Si-doping concentration in the upper QW should be equal to or higher than 1.5×10^{17} cm^{-3}. We noticed that the average distance between doped Si atoms at 1.5×10^{17} cm^{-3} reaches as large as 19 nm. Since this distance is larger than the Bohr radius of Si donor level in GaAs, Si donors may remain localized without contributing to the metal-like conduction. Another important message of this work is that the lower QW should be a GaAs layer without Aluminum, since the small composition of Al in the lower QW substantially degrades the detector performance. This is because n_L is dramatically reduced due to alloy scattering. For future improvements, Si-doping into the upper QW should be finely adjusted in accordance with $\varepsilon_1 < \varepsilon_F < \varepsilon_c < \varepsilon_2$.

In this work, the sensitivity of the THz-CSIP has improved by more than one order of magnitude from the earlier experiments. We also found proper conditions of Si-doping concentration in the upper QW and of the lower QW for further improvement of THz-CSIP.

Acknowledgements

I am very grateful to my supervisor Prof. Takao Nakagawa for giving me a great opportunity to study and research in Institute of Space and Astronautical Science (ISAS/JAXA) and University of Tokyo.

I especially would like to express my deepest appreciation to Prof. Susumu Komiyama for his elaborated guidance, considerable encouragement and invaluable discussion that make my research fruitful and my study life unforgettable. Without his help, this paper would not have been possible. I would like to express my sincere gratitude to Associate Prof. Mitsunobu Kawada for giving me constructive comments and warm encouragement. I also would like to offer my special thanks to Assistant Prof. Yasuo Doi for providing me the present study opportunity. My heartfelt appreciation goes to Assistant Prof. Shuji Matsuura for valuable guidance for my research activity. I would like to show my appreciation to all LIRA members.

Takashi Satoh, and Dr. Sunmi Kim are key members in my work. They have given me the advice and support for experiment and device fabrication. I am deeply grateful to Dr. Mikhail Patrashin at National Institute of Information and Communications Technology (NICT) for supporting CSIP wafer growths for a lot of times. I thank particularly Associate Prof. Yusuke Kajihara for permission to use his laboratory for my study activity since June of 2014.

Finally I would like to offer my special thanks to my family for their understanding, support, encouragement throughout my study.

References

[1] S. Komiyama. “Single-photon detectors in the terahertz range”. *Selected Topics in Quantum Electronics, IEEE Journal of*, 17(1):54–66, 2011.

[2] B.T. Soifer, D.B. Sanders, G. Neugebauer, G.E. Danielson, C.J. Lonsdale, B.F. Madore, and S.E. Persson. “The luminosity function and space density of the most luminous galaxies in the IRAS survey”. *The Astrophysical Journal*, 303:L41–L44, 1986.

[3] L. Spinoglio, K.M. Dasyra, A. Franceschini, C. Gruppioni, E. Valiante, and K. Isaak. “Far-IR/Submillimeter spectroscopic cosmological surveys: predictions of infrared line luminosity functions for z¡ 4 galaxies”. *The Astrophysical Journal*, 745(2):171, 2012.

[4] G. Neugebauer, H.J. Habing, R. Van Duinen, H.H. Aumann, B. Baud, C.A. Beichman, D.A. Beintema, N. Boggess, P.E. Clegg, T. De Jong, et al. “The infrared astronomical satellite (IRAS) mission”. *The Astrophysical Journal*, 278:L1–L6, 1984.

[5] M.F. Kessler, J.A. Steinz, M.E. Anderegg, J. Clavel, G. Drechsel, P. Estaria, J. Faelker, J.R. Riedinger, A. Robson, B.G. Taylor, et al. “The Infrared Space Observatory (ISO) mission”. *Astronomy and Astrophysics*, 315:L27–L31, 1996.

[6] M.W. Werner, T.L. Roellig, F.J. Low, G.H. Rieke, M. Rieke, W.F. Hoffmann, E. Young, J.R. Houck, B. Brandl, G.G. Fazio, et al. “The Spitzer space telescope mission”. *The Astrophysical Journal Supplement Series*, 154(1):1, 2004.

[7] H. Murakami, H. Baba, P. Barthel, D.L. Clements, M. Cohen, Y. Doi, K. Enya, E. Figueredo, N. Fujishiro, H. Fujiwara, et al. “The infrared astronomical mission AKARI”. *Publications of the Astronomical Society of Japan*, 59(sp2):S369–S376, 2007.

[8] G.L. Pilbratt, J.R. Riedinger, T. Passvogel, G. Crone, D. Doyle, U. Gageur, A.M. Heras, C. Jewell, L. Metcalfe, S. Ott, et al. “Herschel Space Observatory: An ESA facility for far-infrared and submillimetre astronomy”. *Astronomy and astrophysics*, 518(1), 2010.

[9] K. Malfait, C. Waelkens, J. Bouwman, A. De Koter, and L.B.F.M. Waters. “The ISO spectrum of the young star HD 142527”. *Astronomy and Astrophysics*, 345:181–186, 1999.

[10] R.G. Smith, G. Robinson, and A.R. Hyland. “Molecular Ices as Temperature Indicators in the Interstellar Medium”. In *Proceedings of the Astronomical Society of Australia*, volume 10, page 241, 1993.

[11] Y. Inoue. “High Energy Gamma-ray Absorption and Cascade Emission in Nearby Starburst Galaxies”. *The Astrophysical Journal*, 728(1):11, 2011.

[12] T. Ueda, S. Komiyama, Z. An, N. Nagai, and K. Hirakawa. “Temperature dependence of the performance of charge-sensitive infrared phototransistors”. *Journal of Applied Physics*, 105(6):064517–064517, 2009.

[13] A. Rogalski and F. Sizov. "Terahertz detectors and focal plane arrays". *Opto-electronics review*, 19(3):346–404, 2011.

[14] Z. An, T. Ueda, J.C. Chen, S. Komiyama, and K. Hirakawa. "A sensitive double quantum well infrared phototransistor". *Journal of applied physics*, 100(4):044509, 2006.

[15] P. Nickels, S. Matsuda, T. Ueda, Z. An, and S. Komiyama. "Metal hole arrays as resonant photo-coupler for charge sensitive infrared phototransistors". *IEEE J. Quantum Electron.*, 46(3):384–390, 2010.

[16] K.L. Campman, H. Schmidt, A. Imamoglu, and A.C. Gossard. "Interface roughness and alloy-disorder scattering contributions to intersubband transition linewidths". *Applied physics letters*, 69(17):2554–2556, 1996.

[17] T. Unuma, T. Takahashi, T. Noda, M. Yoshita, H. Sakaki, M. Baba, and H. Akiyama. "Effects of interface roughness and phonon scattering on intersubband absorption linewidth in a GaAs quantum well". *Applied Physics Letters*, 78(22):3448–3450, 2001.

[18] H. Lüth. *"Solid surfaces, interfaces and thin films"*, volume 4. Springer, 2001.

[19] G. Irmer, M. Wenzel, and J. Monecke. "The temperature dependence of the LO (Γ) and TO (Γ) phonons in GaAs and InP". *physica status solidi (b)*, 195(1):85–95, 1996.

[20] V.Y. Davydov, Y.E. Kitaev, I.N. Goncharuk, A.N. Smirnov, J. Graul, O. Semchinova, D. Uffmann, M.B. Smirnov, A.P. Mirgorodsky, and R.A. Evarestov. "Phonon dispersion and Raman scattering in hexagonal GaN and AlN". *Physical Review B*, 58(19):12899, 1998.

[21] J.C. Cao, Y.L. Chen, and H.C. Liu. "Effect of optical phonons on the spectral shape of terahertz quantum-well photodetectors". *Superlattices and Microstructures*, 40(2):119–124, 2006.

[22] R. Nihei, K. Nishimura, M. Kawada, S. Matsuura, Y. Doi, T. Satoh, and S. Komiyama. "Development of an ultra-sensitive far-infrared detector based on double quantum-well structure". *the ISSTT proceedings*, 23(3):32, 2012.

[23] P. Khosropanah, R. Hijmering, M. Ridder, J.R. Gao, D. Morozov, P.D. Mauskopf, N. Trappe, C. O'Sullivan, A. Murphy, D. Griffin, et al. "TES Arrays for the Short Wavelength Band of the SAFARI Instrument on SPICA". In *SPIE Astronomical Telescopes+ Instrumentation*, pages 845209–845209. International Society for Optics and Photonics, 2012.

[24] A. Mooradian and A.L. McWhorter. "Polarization and intensity of Raman scattering from plasmons and phonons in gallium arsenide". *Physical Review Letters*, 19(15):849, 1967.

[25] C.R. Pidgeon. "Handbook on Semiconductors". *Vol 2North-Holland*, page 223, 1980.

[26] E.J. Johnson and D.M. Larsen. "Polaron induced anomalies in the interband magnetoabsorption of InSb". *Physical Review Letters*, 16(15):655, 1966.

[27] J.A. Kash, J.C. Tsang, and J.M. Hvam. "Subpicosecond time-resolved Raman spectroscopy of LO phonons in GaAs". *Physical review letters*, 54(19):2151, 1985.

[28] H.C. Liu, C.Y. Song, Z.R. Wasilewski, A.J. SpringThorpe, J.C. Cao, C. Dharma-Wardana, G.C. Aers, D.J. Lockwood, and J.A. Gupta. "Coupled electron-phonon modes in optically pumped resonant intersubband lasers". *Physical review letters*, 90(7):077402, 2003.

[29] Manfred Helm. "The basic physics of intersubband transitions". *Semiconductors and semimetals*, 62, 1999.

[30] S. De Liberato and C. Ciuti. "Quantum theory of intersubband polarons". *Physical Review B*, 85(12):125302, 2012.

[31] S. Hameau, Y. Guldner, O. Verzelen, R. Ferreira, G. Bastard, J. Zeman, A. Lemaitre, and J.M. Gérard. "Strong electron-phonon coupling regime in quantum dots: evidence for everlasting resonant polarons". *Physical review letters*, 83(20):4152, 1999.

[32] T. Ueda, Y. Soh, N. Nagai, S. Komiyama, and H. Kubota. "Charge-Sensitive Infrared Phototransistors Developed in the Wavelength Range of 10–50 m". *Japanese Journal of Applied Physics*, 50:020208, 2011.

[33] Y. Kajihara, K. Kosaka, and S. Komiyama. "Thermally excited near-field radiation and far-field interference". *Optics express*, 19(8):7695–7704, 2011.

[34] Z. Wang, S. Komiyama, T. Ueda, M. Patrashin, and I. Hosako. "Charge sensitive infrared phototransistor for 45 μm wavelength". *Journal of Applied Physics*, 107(9):094508–094508, 2010.

[35] R. Nihei, S. Komiyama, M. Kawada, S. Matsuura, Y. Doi, T. Satoh, and T. Nakagawa. "Development of Charge Sensitive Infrared Phototransistors for the Far-Infrared Wavelength". *Journal of Low Temperature Physics*, pages 1–6, 2014.